NANOCARVING OF TITANIA SURFACES USING HYDROGEN BEARING GASES

A Thesis
Presented to
The Academic Faculty

By

Helene Rick

In Partial Fulfillment
Of the Requirements for the Degree
Master of Science in Materials Science and Engineering

Georgia Institute of Technology

August 2005

NANOCARVING OF TITANIA SURFACES USING HYDROGEN BEARING GASES

Approved by:

Dr. Kenneth H. Sandhage, Chair
School of Materials Science and Engineering
Georgia Institute of Technology

Dr. Sheikh Akbar
School of Materials Science and Engineering
Ohio State University

Dr. Bob Snyder
School of Materials Science and Engineering
Georgia Institute of Technology

Approved Date: May 9th, 2005

ACKNOWLEDGEMENT

Many, many people have helped keep me focused during the development of this thesis. Dr. Kenneth H. Sandhage, my advisor, provided a motivating, enthusiastic, and critical atmosphere during the many discussions we had. It was a great pleasure to conduct this thesis under his supervision. I also acknowledge Dr. Sheikh Akbar and Sehoon Yoo, at Ohio State University, who provided constructive comments and invaluable insight to my project throughout my investigation. Not to mention Sehoon Yoo's original research, making this thesis possible.

Next, I would like to thank my colleagues in the Sandhage group for their support and contributions to my thesis. Although they have all contributed in one way or another I would like to take the time to thank a few of them individually. Sam Shian was especially helpful in bringing my work into the 20^{th} century through the use of computers to gather and record data. Without his help I would still sitting next to my furnace, scribbling down data points. Mike Weatherspoon organized many study sessions, thereby motivating me to study and learn; and Shawn Allan listened to my ramblings about my research and helped me brainstorm. Finally, I would like to thank Ben Church for taking the time to read and revise my thesis prior to its submission to my advisor and the thesis committee.

Needless to say, I am grateful to all of the faculty and staff of the Materials Science and Engineering department for helping to make this possible. I am especially

indebted to Susan Bowman, academic advisor, and Mechelle Kitchings, accountant, for making sure I had the tools necessary to complete my degree.

Finally, my most heartfelt thanks goes to my fiancée Christian and my family. Ohne ihre Hilfe, Toleranz und ständige Aufmunterung wäre diese Arbeit nie beendet worden.

TABLE OF CONTENTS

LIST OF TABLES

LIST OF FIGURES

LIST OF SYMBOLS OR ABBREVIATIONS

Inductively Coupled Plasma	ICP
Argon	Ar
Energy Dispersive Spectroscopy	EDS
Hydrogen	H_2
Mass Spectrometry	MS
Methane	CH_3
Nitrogen	N_2
Scanning Electron Microscopy or Microscope	SEM
Standard Cubic Centimeters per Minute	sccm
Standard Liter per Minute	slpm
Thermogravimetric Analysis	TGA
Titanium Dioxide	TiO_2
Transmission Electron Microscopy	TEM
X-ray Diffraction	XRD
Zirconium	Zr

SUMMARY

An investigation of surface structures formed on polycrystalline and single crystal TiO_2 (titania) samples having under gone various heat treatments in a controlled hydrogen bearing atmosphere was conducted. The study included the recreation and examination of the process discovered by Sehoon Yoo at Ohio State University to form nanofibers on the surface of polycrystalline TiO_2 disks. Fibers were formed by heating samples to 700°C in a 5%H_2 95%N_2 gas stream. The nanofibers formed during this processes are approximately 5-20 nanometers in diameter and can be 100's of nanometers long. The fibers do not actually grow on the surface, but are what remain of the surface as the material around them is removed by the gas stream – i.e., nanocarving. The mechanism of fiber formation and the effect of varying experimental parameters remained unknown and were explored within this study. This included changing gas composition, flow rate, and changes in sample preparation. The effect of isovalent doping and impurities within the starting powder were examined. Sintering temperature and time was investigated to determine the effect of grain size and surface morphologies prior to nanocarving. The effect of elevated temperature and 5%H_2 95%N gas on the surface of TiO_2 single-crystal wafers was also investigated. Test methods include Thermogravimetric Analysis (TGA), Mass Spectrometry (MS), Scanning Electron Microscopy (SEM), and X-ray diffraction (XRD) analysis.

CHAPTER 1

INTRODUCTION

TiO_2 is one of the most studied metal oxide systems. The motivation for most of the research in this area is its wide range of applications. TiO_2 is regularly used as a photocatalyst in solar cells, as a gas sensor, as a white pigment, and as an optical coating in many electronic device [1]. Photocatalytic decomposition of organics and photocleavage of water on the surface of TiO_2 has recently received a large amount of interest [2]. By obtaining an understanding of the properties of TiO_2 on a fundamental level improved processing of raw materials and performance of end devices can be achieved. The structure of TiO_2 in the bulk and more importantly on the surface is responsible for its behavior in many "high tech" applications, and, therefore, it is important to be able to alter the surface as desired.

Recently one-dimensional nanostructures of metal oxides and materials in general have become the focus of intense research due to the potential new applications in the electronics, photonics, and sensor industries that such structures could enable [3]. Difficulty lies in the ability to produce such structures in mass and still maintain control of the dimensions on the nanometer scale. The fabrication of TiO_2 nanostructures has received much attention in this new area because the combination of its unique properties and the high surface areas of nanostructures has the potential of increasing the performance efficiencies of solar cells, sensors, and purification systems [1, 3-5]. A

novel and simple new process to fabricate nanofibers on the surface of rutile, TiO_2 disks by reacting with a hydrogen bearing gas was discovered by Yoo *et al* [6]. The surface of the disks was covered with oriented arrays of fibers that had been carved out of the surface. Transmission electron microscopy (TEM) determined that the fibers were oriented along the (001) direction of the rutile structure [6]. The amazing simplicity of this process, which has been coined "nanocarving", makes it a viable option for large-scale production. Since the fibers are formed on TiO_2 in the rutile phase, a brief overview of the structure of this phase will be given.

TiO_2 can form three different crystalline phases: rutile, anatase, and brookite. Although other structures have been discovered, anatase and rutile are typically used for most applications of TiO_2 [1]. The rutile phase is the thermodynamically stable phase at high temperatures. Its unit cell is tetragonal; it is composed of a titanium atom surrounded by 6 oxygen atoms in a distorted octahedral configuration [1]. Figure 1.1 illustrates how these octahedra are orientated with respect to one another and the unit cell

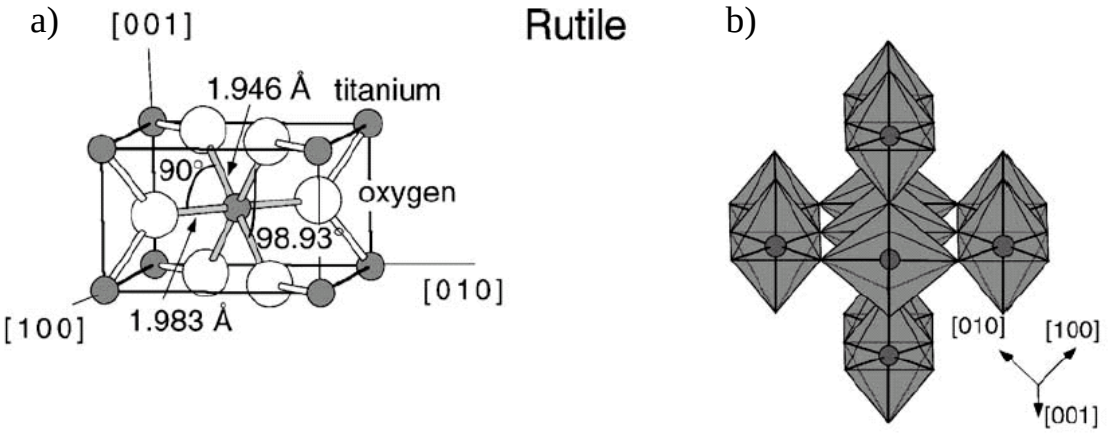

Figure 1.1: Schematics of the rutile unit cell (a) and the orientation of the distorted octahedra (b) for the rutile phase in TiO_2 after ref. [1].

they create in the rutile structure. The arrangement of the octahedrons leads to open channels parallel to the c-axis of the unit cell. These channels can be seen when looking at the (001) surface as illustrated in Figure 1.2. It is theorized by Yoo et al. that these channels play a significant role in nanofiber formation and orientation by providing enhanced paths for diffusion [6, 7]. The significance of this structure in the formation of nanofibers and, therefore, the effect of doping on the fiber formation will be discussed further in Chapters 2 and 3.

The focus of this investigation was to determine the effect on the fibers of altering nanocarving conditions, including the composition of the starting powder for

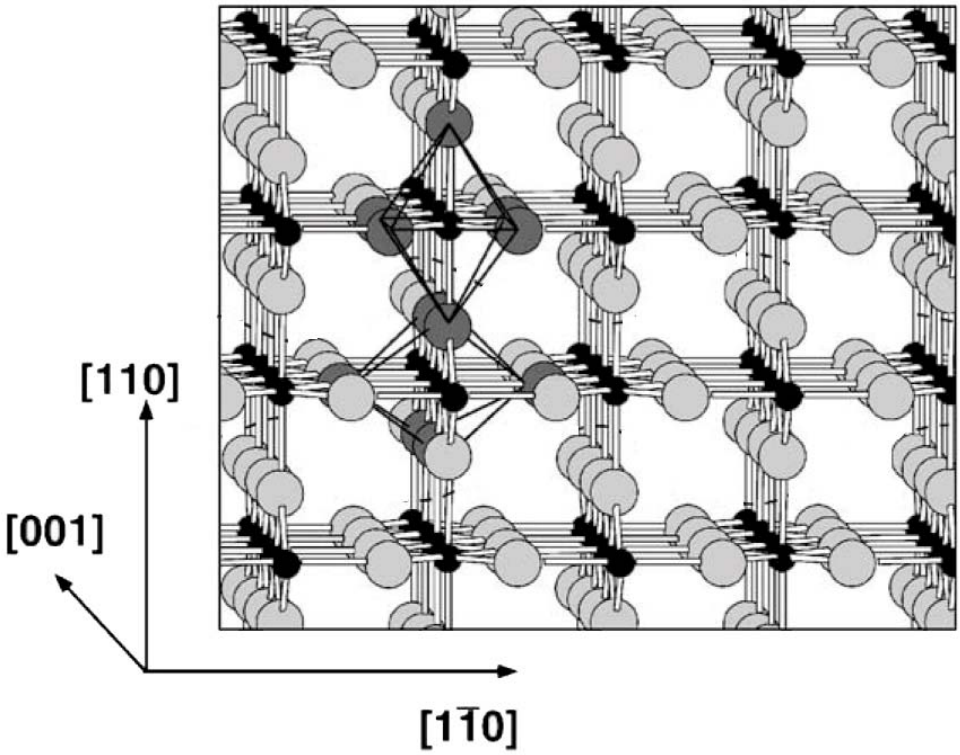

Figure 1.2: Ball and stick schematic of the (001) face of the rutile phase structure in TiO_2. The distorted octahedrons are aligned in 2 perpendicular directions, forming open channels parallel to the <001> direction after ref. [1].

polycrystalline samples, and to determine whether this process can be used to form nanofibers on single crystal TiO_2 wafers. Both chapters 2 and 3 address nanofiber formation on polycrystalline TiO_2 disks. Chapter 4 will address the effect of nanocarving at higher temperatures on single crystalline TiO_2(001) wafers.

CHAPTER 2

INVESTIGATION OF THE TITANIUM SOLID-STATE DIFFUSION THEORY OF NANOFIBER FORMATION ON TIO_2 DISKS

2.1 Introduction

Titanium dioxide (TiO_2) is a widely researched material due to its unique chemical, electrical, and optical properties. TiO_2 is chemically stable, nontoxic, and inexpensive. Its applications range from a commonly used white pigment due to its high refractive index to possible use as a solar energy conversion surface owing to its ability to catalyze the splitting of water [8]. The thermodynamically stable form of TiO_2, rutile, has many promising industrial applications such as semiconductor electrodes for the photoelectrolysis of water and as an oxygen sensor. Surface structures and atomic defects/impurities can significantly influence the properties of TiO_2 [9].

Recently, a significant level of research has focused on the creation of nanostructured devices due to their potential applications in a variety of areas including photonics, electronics, and sensing [3, 4]. Precisely controlling the dimensions of such devices or their components down to the nanometer scale has proven to be quite complicated; still, some promising techniques have been discovered. Yoo *et al.* reported on the formation of nanofibers on the surface of TiO_2 polycrystalline disks using a simple production method [6]. By flowing a hydrogen bearing gas over the surface of polycrystalline TiO_2 at an elevated temperature (700°C), nanofibers oriented along the c axis of the rutile structure grew over the entire surface [6].

Recent developments in the study of TiO_2 nanocarving have led to a working theory behind fiber formation. Yoo *et al.* have reported on a titanium solid-state diffusion theory to explain fiber formation as illustrated in Figure 2.1 [7]. The reaction between the H_2 gas and the TiO_2 disk can be described by the following chemical equation:

$$TiO_2 + xH_2(g) \rightarrow TiO_{2-x} + xH_2O(g)$$

The above equation implies that the surface of the disks and the composition of the fibers would not remain stoichiometric TiO_2, but some reduced form, such as Ti_2O_3 or TiO. Using XRD, XPS, and TEM it was determined that this was not the case [6]. This can be explained through the solid-state diffusion of Ti^{3+} interstitials down the open

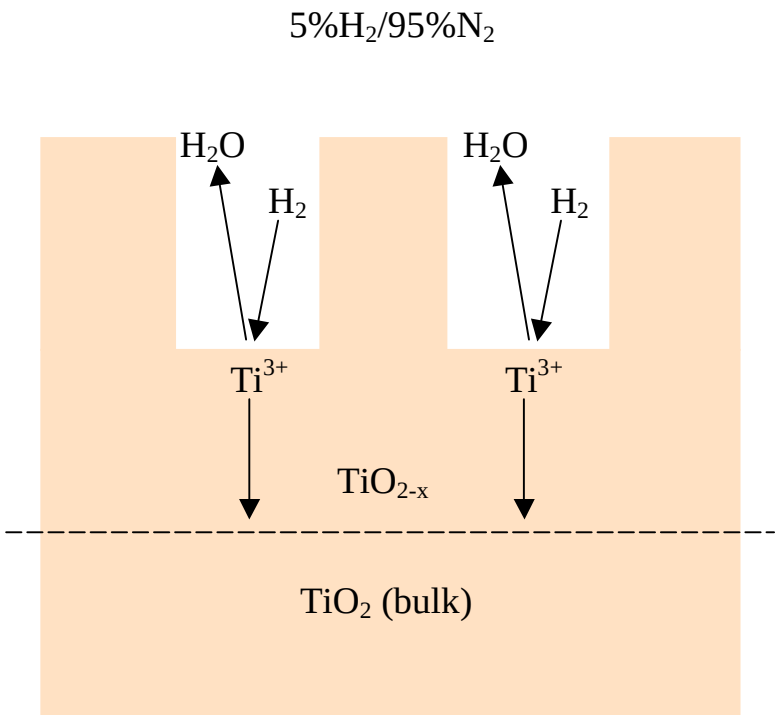

Figure 2.1: Schematic of titanium solid-state diffusion theory proposed by Yoo *et al.* illustrating the nanofiber formation process [7].

channels in the c-axis of the rutile structure [10]. However, it is also possible that titanium is being removed in the form of a volatile species. This study focuses on investigating the validity of the titanium solid-state diffusion theory proposed by Yoo *et al* [6].

2.2 Experimental Methods

TiO_2 powder (Anatase, 99.9%, Alfa Aesar, Ward Hill, MA, USA) having average particle size of 32 nm was used to prepare undoped and doped polycrystalline disks. One aliovalent dopant, Fe, was introduced into the TiO_2 powder at a concentration of 0.1 mole -% (i.e., $Ti_{(0.999)}Fe_{(0.001)}0_2$). Iron (III) nitrate hydrate $Fe(NO_3)_3 \bullet 9H_2O$ (Puratronic, 99.999%, metal basis, Alfa Aesar, Ward Hill, MA, USA) was used to dope TiO_2 powders. The final Fe_2O_3 content of the starting solution ($Fe(NO_3)_3 \bullet 9H_2O$) was determined using thermograviometeric analysis (Jupiter 449c, Netzsch, Germany). The starting solution was weighed, placed in Al_2O_3 crucible, and heated to 1000°C (10 °C/min) to burn off all organic compounds. The concentration of Fe_2O_3 in the raw starting material was determined to have been 20 weight-percent.

Iron (III) nitrate hydrate was dissolved in anhydrous ethanol (Fisher, USA) and TiO_2 powder was added to the solution in different amounts to obtain the desired 0.1-mole % doping level. TiO_2 containing solution was stirred for 2 h to allow for uniform mixing. Hydrolysis of the Iron (III) nitrate hydrate was achieved by slowly (1 ml/min) adding excess amounts (10 ml) of deionized (DI) water (NANOpure Diamond Life Science (UV/UF), 18.2 MΩ-cm resistivity H_2O, 0.2 μm filtered, Barnstead International,

Dubuque, Iowa) to the solution while vigorously stirring. Under continuous stirring the solution was heated to 60°C and allowed to dry for 24 h.

Dried doped powders were placed in a titanium tube (Grade 2 purity in accordance with ASTM B338-05a) and calcined in a horizontal tube furnace (Lindberg/Blue M Tube Furnace, Asheville, NC, USA) in air at 600°C for 1 hour at a heating rate of 5-10°C per minute. To break up agglomerates, powders were mixed with high purity acetone and ground using a granite mortar and pestle. Powders were sieved through 170-mesh sieve to eliminate larger particles found in calcined powder so as to achieve increased density in the final sintered product. Both doped and undoped powders were pressed into disks using a 12.7 mm diameter stainless steel die (Carver, Inc, Wabash, IN, USA). The peak stress reached during uniaxial pressing was 75-400 MPa. The disks were sintered in air using a 5-10°C/min heating rate to a set temperature of 1200°C followed by a 0-8 h hold time. The disks were allowed to furnace cool from the hold temperature, i.e. disks were not removed from the furnace to cool. X-ray diffraction analyses (PW 1800 X-ray Diffractometer, Phillips, USA) were preformed on doped samples to what phases were present. The XRD patterns were obtained using Cu-Kα1 radiation at 40 kV and 30 mA with a scan rate of 0.020° step/sec from 20° to 80°.

A linear intercept analysis of SEM images was used to determine the grain size of doped and undoped samples after ASTM E112-96(2002). Two samples of each different sintering hold time, doped, and undoped disks were imaged in 4 areas at 2,000x. Each area was divided into 5 separate areas having 5 horizontal lines (~ 25 μm long and 5 μm apart) for a total of 40 inspection areas (~ 5000 grains) per sample pair.

Individual disks were placed in a horizontal tube furnace (Lindberg/Blue M Tube Furnace, Asheville, NC, USA) as shown in Figure 2.2. After securing o-ring sealed aluminum end-caps at both ends of the quartz tube in the furnace, a mixed gas containing 1-10% H_2 or 5% CH_3 as a reactant gas and either N_2 or Ar as a carrier gas were passed over the sample at a flow rate of 1 slpm upon heating of the furnace. A typical furnace run consisted a 5-10°C/min heating rate to a set temperature of 700°C followed by an 8 h hold. Samples were allowed to furnace cool from the hold temperature; atmospheric control was maintained at a flow rate of 1 slpm throughout the run.

Mass spectroscopy was used to analyze the exhaust gases from the furnace reaction tube. Two samples were placed into a quartz tube in a horizontal tube furnace. Each end of the quartz tube was sealed using o-ring sealed aluminum end caps. 5%H_2 95%N_2 gas was passed over the samples at 1slpm as the furnace was heated to 700°C, as

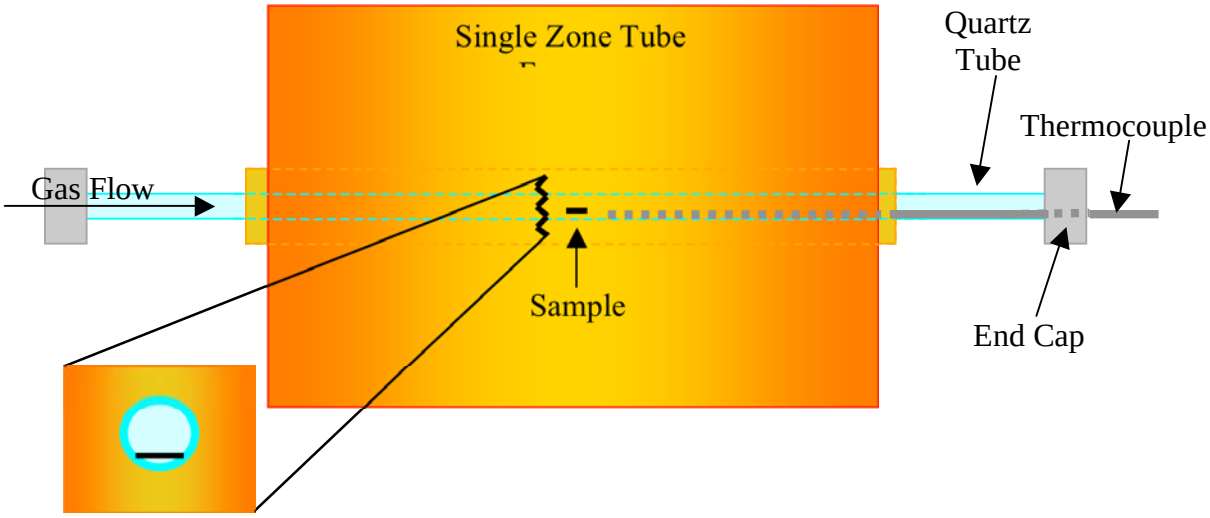

Figure 2.2: Schematic of the furnace set up used for the etching process. A 1" diameter x 5' long quartz tube was placed inside a 3" diameter x 3' long alumina tube in a 3" tube furnace. The large furnace provided a longer hot zone than would be found in a 1" tube furnace.

described earlier. The exhaust gas was split using a tee in the exhaust line (1/4" stainless steel tubing and fittings). One stream of gas was connected to a gas analysis system (QIC-20 Gas Analysis System, HIDEN Analytical, England) in mass mode using a secondary electron multiplier (SEM) at a flow rate of 20 sccm, and the other stream was sent to an oil bubbler and exhausted to a fume hood. The quartz tube and gas lines outside of the furnace at the exiting end were heated to 120°C using heating tape to eliminate condensation of possible volatile TiO_2-containing gases prior to reaching the gas analysis system. Inductively Coupled Plasma (ICP) analyses were conducted (Gene Weeks, Research Coordinator I, Laboratory for Environmental Analysis, University of Georgia Athens) on cotton swabs used to swab the inside of the reaction tube.

2.3 Results

The data collected can be categorized into several investigations. The effect of grain size, variation in the type of reaction gas, the effect of Fe-doping on the etching process, and the analysis of exhaust gases were all investigated.

2.3.1 Grain Size Effects

The sintering time at 1200°C was varied to influence grain size (as opposed to varying sintering temperatures). Sintering times and corresponding grain sizes are listed in Table 2.1. Figure 2.3 illustrates the difference in grain sizes (1.12 μm, 2.22 μm, 2.72 μm, and 3.43 μm) of several undoped TiO_2 disks.

Table 2.1. Tabulation of the variation of grain size (± standard deviation) produced by varying sintering hold times.

Sintering hold time at 1200°C (h)	Average grain size (μm)	Density (% Theoretical)
0	1.12 ± 0.04	92.5
1	2.22 ± 0.10	92.3
2	2.34 ± 0.12	92.5
6	2.64 ± 0.27	92.7
12	2.72 ± 0.29	95.3
48	3.43 ± 0.31	94.9

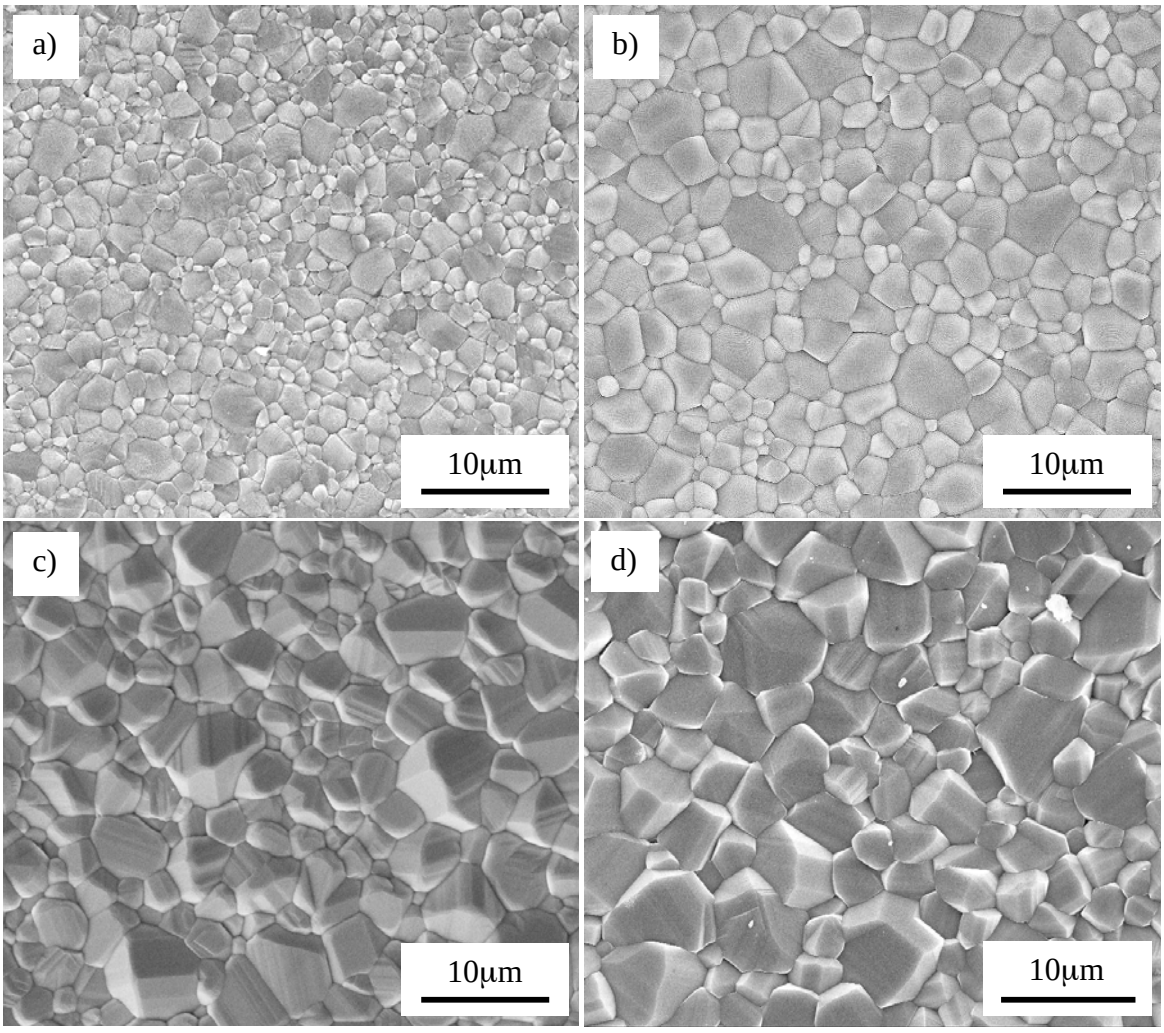

Figure 2.3: SEM images of the surfaces of undoped TiO_2 disks after sintering at 1200°C for a hold time of (a) 0 hours, (b) 1 hours, (c) 12 hours, and (d) 48 hours.

Samples were etched using a 5%H_2 95%N_2 gas mixture at 700°C for 8 h. SEM images of several different grain size samples after etching for 8 h are shown in Figure 2.4. Differences in the etched nanostructures are evident when comparing the smallest grain sample (Figure 2.4a) to the largest grain sample (Figure 2.4d). The small grain samples exhibited extensive fiber formation on the surface, whereas the larger grain size samples showed less extensive fiber formation.

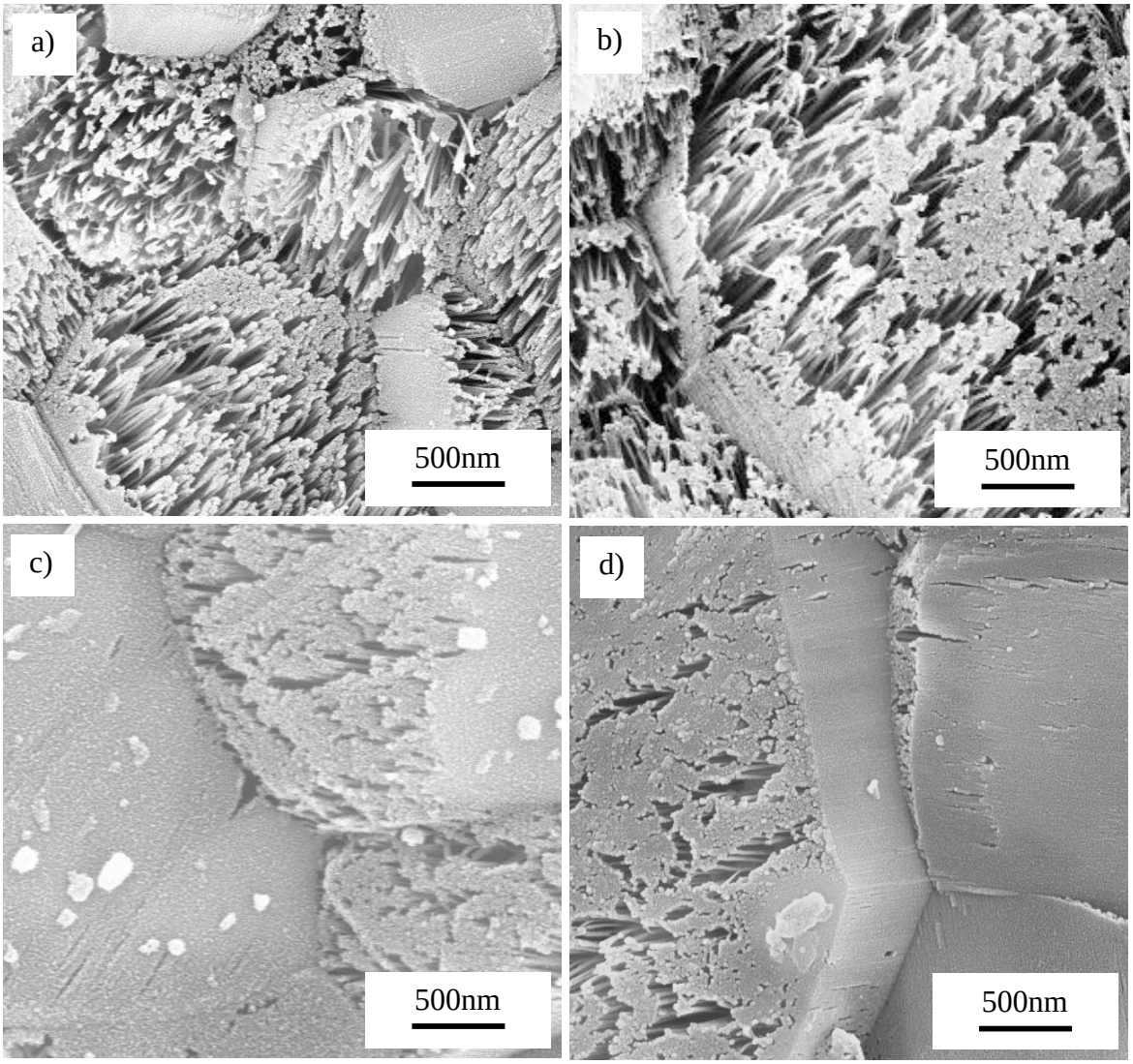

Figure 2.4: SEM images of the surface of undoped TiO_2 disks after sintering at 1200°C for a hold time of (a) 0 hours, (b) 1 hours, (c) 12 hours, and (d) 48 hours followed by exposure to a flowing 5%H_2 95%N_2 gas mixture for 8 h at 700°C.

2.3.2 Effect of Varying the Reaction Gas

Various gases were investigated in etching to determine the role of the inert gases, the concentration of H_2, and the type of reducing gas on the formation of nanofibers. Included in the study were the following mixtures: 1%H_2 99%N_2, 5%H_2 95%N_2, 10%H_2 90%N_2, 4%H_2 96%Ar, and 5%CH_3 95%N_2. Samples were exposed to these various gas mixtures at a flow rate of 1 slpm for 2-8 h at 700°C. The TiO_2 disks possessed an average grain size of 2.34 μm.

Images of the disk surfaces after etching for 8 h using 5%H_2 95%N and 4%H_2 96%Ar can be seen in Figure 2.5. No apparent qualitative difference in the nanofibers was observed. The average diameter and the amount of fibers remained the same for both inert gases.

Methane, a different reducing gas, was used to etch TiO_2 disks. Disks etched using 5%CH_3 95%N did not exhibit appreciable nanofiber formation, as illustrated in

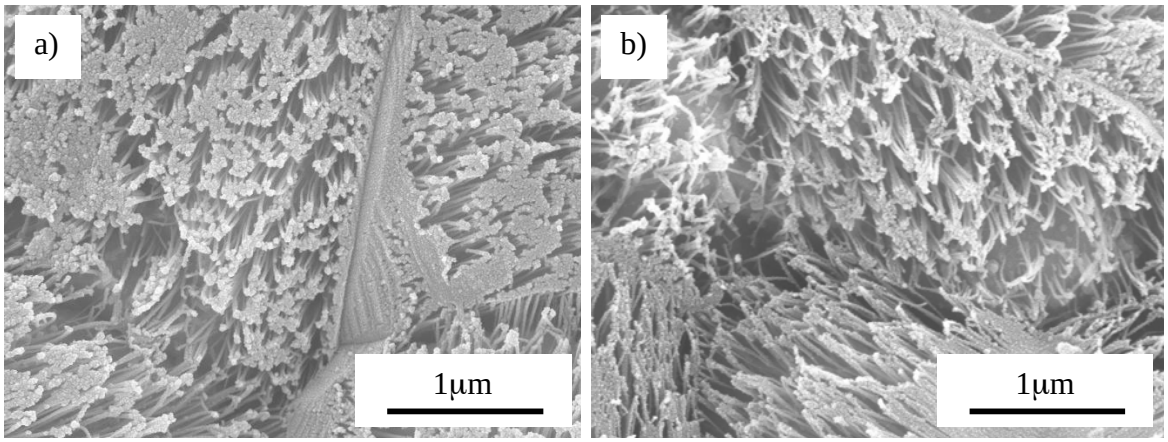

Figure 2.5: SEM images obtained from the surfaces of TiO_2 disks etched using (a) 4%H_2 96%Ar and (b) 5%H_2 95%N_2 gas mixtures.

Figure 2.6. A small amount of nanofibers was observed at only relatively few locations (Figure 2.6b).

2.3.3 MS and ICP Analyses of Reaction Products

Exhaust gases from the nanocarving processes were analyzed by mass spectroscopy (MS). Gases were analyzed for 7 h of the etching process. Figure 2.7 shows a MS spectrum taken after 1 h of etching; it is representative of the entire process. Major peaks located at 28 and 44 amu correspond to N_2 and CO_2, respectively. The small peak at 29 amu adjacent to the N_2 peak was due to one of its most common N_2 isotopes. The smaller peaks, just below that of CO_2, at 40 amu and 42 amu correspond to C_2H_2N (nitrile) and N_3 (nitrogen cations). Since titanium has a molecular weight of approximately 48 amu and no peaks were detected past 44 amu, it can be concluded that no gaseous form of titanium had formed.

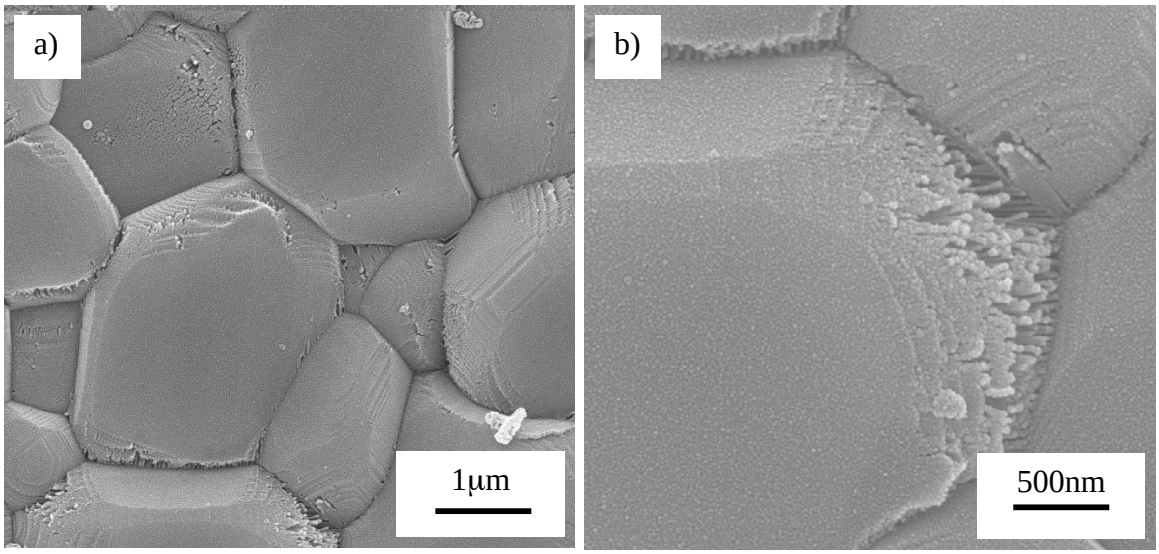

Figure 2.6: SEM images of the surface of TiO_2 disks after etching at 700°C for 8 h using 5%CH_3 95%N_2. At a distance (a) it appears no fiber formation occurred. However, on closer inspection (b), a minimal amount of nanocarving was noticeable.

Ti-bearing gas species may have condensed at the cooler end of the reaction tube, upstream of the mass spectrometer. To evaluate this possibility, cotton swabs were used to swab the interior of the reaction afterwards. ICP analysis of those cotton swabs indicated that no extra TiO_2 was present than in the unused control cotton swabs. Results of such ICP analyses are listed in Table 2.2.

Table 2.2. Amount of titanium present in cotton swabs used to swab out reaction tube and unused cotton swabs.

Sample	Ti content (ppm)
Used cotton swab a	59.2
Used cotton swab b	46.7
Unused cotton swab a	54.4
Unused cotton swab b	59.3

2.3.4 Effect of Fe-doping

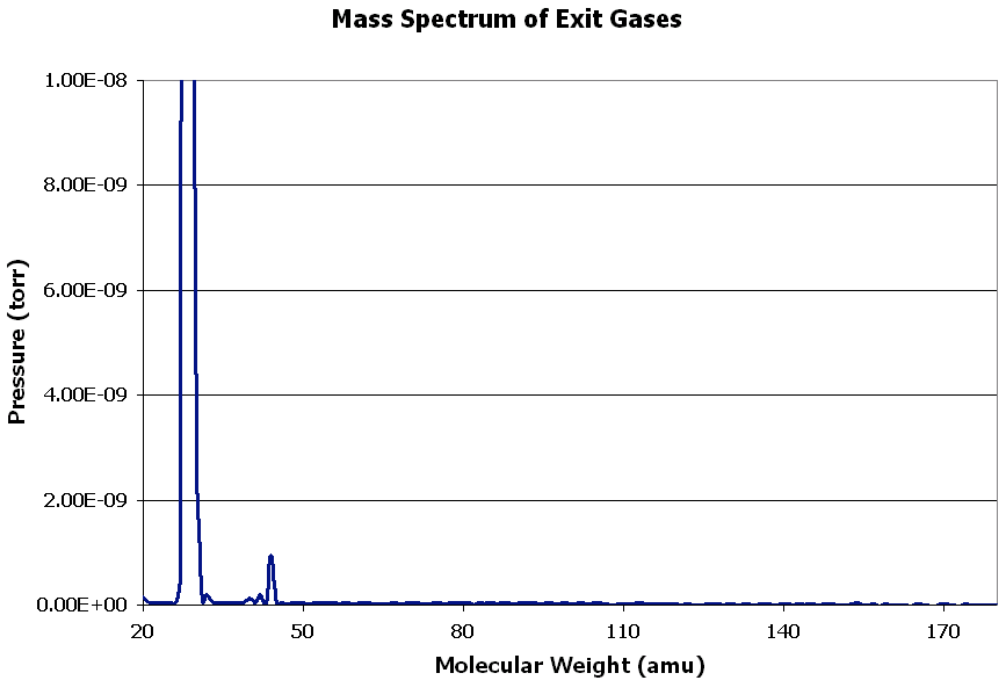

Figure 2.7: Mass spectroscopic analyses of exhaust gases during nanocarving of TiO_2 disks. The peak at 28 amu corresponds to N_2, followed by another smaller peak at 29 amu, which corresponds to a N_2 isotope. A CO_2 peak appears at 44 amu. No molecules containing titanium were detected.

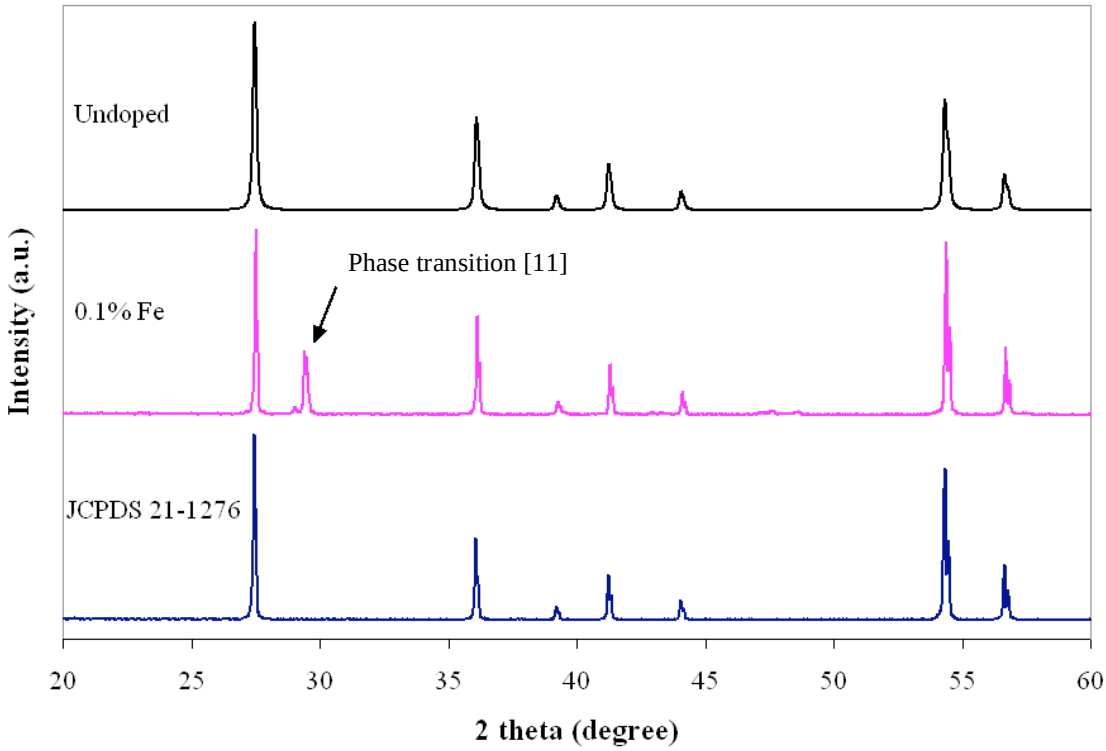

Figure 2.8: The XRD spectrums of undoped disks and 0.1 mole-% Fe-doped disks along with the JCPDS 21-1276 file for rutile TiO_2. The peak at 29° in the 0.1%Fe spectrum is attributed to a phase transition between rutile and anatase [11].

XRD patterns of the doped samples indicated that the sample was rutile TiO_2, however, there was a peak at ~29°, which is attributed to the presence of anatase and rutile as illustrated in Figure 2.8. To investigate the effect of iron on fiber formation, powders were doped with 0.1 mole % Fe. As illustrated in Figure 2.9, nanocarving occurred on both small (2.63 μm) and large (13.28 μm) grain samples. When comparing the amount of fiber formation on large grain Fe-doped samples (Figure 2.9b) and undoped samples (Figure 2.4d) an enormous difference was observed. The Fe-doped samples have a significant amount of fibers on the surface, comparable in density (number of nanofibers per area) to small grain undoped samples. The undoped large

grain samples have a much lower density of nanofibers on the surface, although some fiber formation was observed.

2.4 Discussion

The aforementioned experiments and their results can be used to support the titanium solid-state diffusion theory proposed by Yoo *et al.* Related experiments mentioned above include:

1. Grain size effects
2. Effect of varying reaction gases
3. MS and ICP analyses of reaction products
4. Effect of Fe-doping

The effect of grain size on nanocarving was investigated to help confirm or reject the titanium solid-state diffusion theory proposed by Yoo *et al* [7]. In this theory Yoo *et*

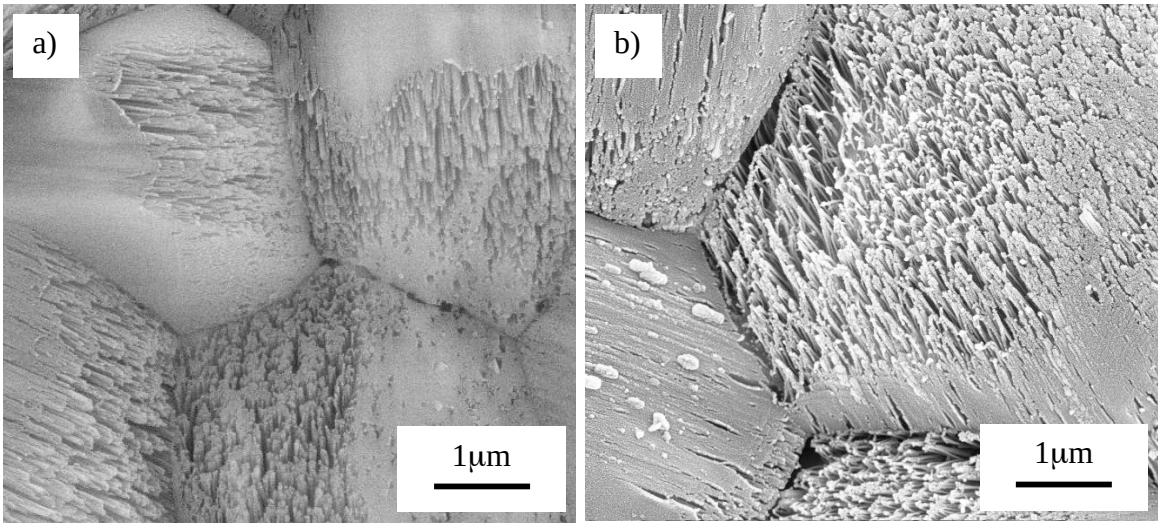

Figure 2.9: SEM images of the surfaces of 0.1 mole % Fe-doped TiO_2 disks having average grain sizes of (a) 2.63 μm and (b) 13.28 μm after etching using 5%H_2 95%N_2 at 1 slpm at 700°C for 8 h.

al. proposed that grain boundaries may act as a fast diffusion path for Ti interstitials and, therefore, the rate of formation of nanofibers may be affected by grain size. As grain size increases, the Ti interstitials would not diffuse into the bulk quickly enough, eventually saturating the area immediately below the surface with Ti and hindering further diffusion and fiber formation. Yoo *et al.* have studied grain size effects by varying the sintering temperature to achieve various grain sizes [7]. Previously, however, it was determined that sintering temperatures higher than 1200°C no longer lead to nanofiber formation as illustrated in Figure 2.10. Although the sintering temperature was only increased for 2 of the 6 h and the increase was less than 7% of the typical (1200°C) sintering temperature, nanofiber formation was hindered. Therefore, to decrease grain size, sintering hold times were shortened. For the shortest sintering time, samples were ramped to 1200°C at 5-10°C/min and the furnace was turned off, allowing samples to immediately start cooling to room temperature (i.e. no hold time at 1200°C). The decrease in fiber formation due to an increase in grain size, Figure 2.4, helps support the titanium solid-state diffusion

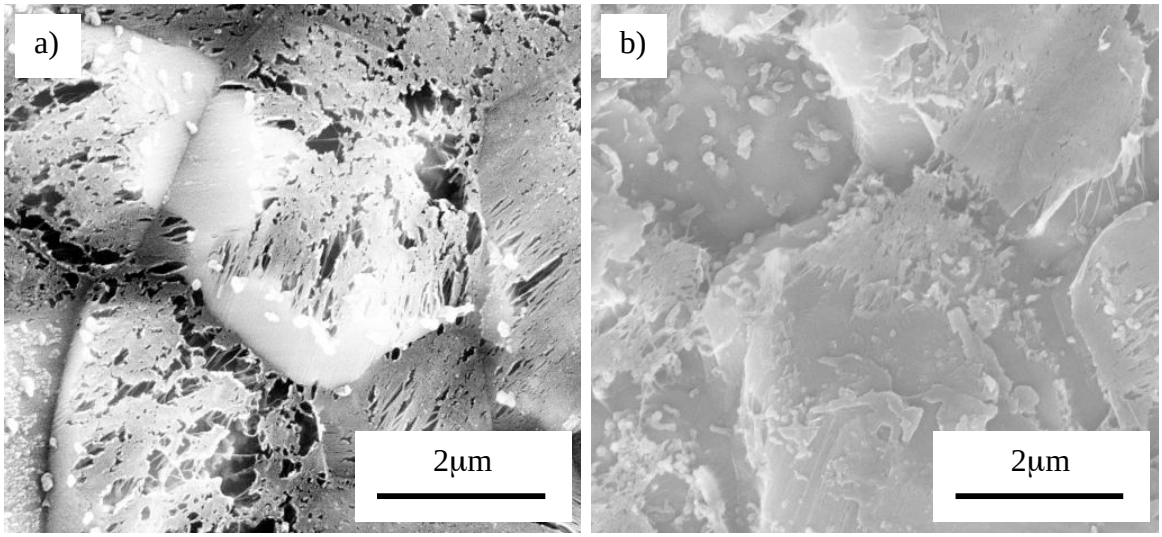

Figure 2.10: SEM images of the surfaces of TiO_2 disks sintered for 2 h at (a) 1225°C and (b) 1275°C followed by 4 h hold at 1200°C, after etching using 5%H_2 95%N_2 at 1 slpm at 700°C for 8 h.

theory. As titanium interstitials are not able to reach a grain boundary quick enough, a chemical gradient arises that impedes titanium diffusion to the bulk and fiber formation ceases. Although this result was consistent with the titanium solid-state diffusion theory, it did not negate the possibility of a volatile gas species containing the titanium atoms laving the surface (i.e., a gas-phase diffusion model). Variation of the reaction gases was necessary to eliminate the involvement of nitrogen in fiber formation. The absence of nitrogen in the gas mixture had little or no effect on fiber formation, as illustrated in Figure 2.5a, where a 4% H_2 96%Ar gas mixture was passed over samples at 1 slpm at 700°C. The extent of fiber formation was similar to the case in which a 5%H_2 95%N_2 gas mixture was utilized. Varying the amount of hydrogen present in the gas stream can be seen to affect the quality of the fibers on the surface (Figure 2.11). Using a 1%H_2 99%N_2 gas mixture for an 8 h etching time led to uniform straight nanofibers, Figure 2.11a. When the hydrogen content was increased to 5% (standard content used) the fibers were relatively straight and long and it appeared that more material had been removed from the surface than for the 1%H_2 case, as illustrated in Figure 2.11b. Increasing the hydrogen content even further to 10% for 8 h appeared to yield little or no fibers formation on the surface (Figure 2.11c). It can be seen that the surface had still been etched, but that no fibers had formed. At short etch times (2 h) using 10% hydrogen gas, fibers were formed on the surface, however, the etch appears to be too aggressive and the nanofibers were not formed uniformly within the grains, Figure 2.11d. Quantitative data has not been collected for this phenomenon, but the possibility exists that hydrogen concentration variations could be used to vary fiber formation density (i.e., the aggressiveness of the etch).

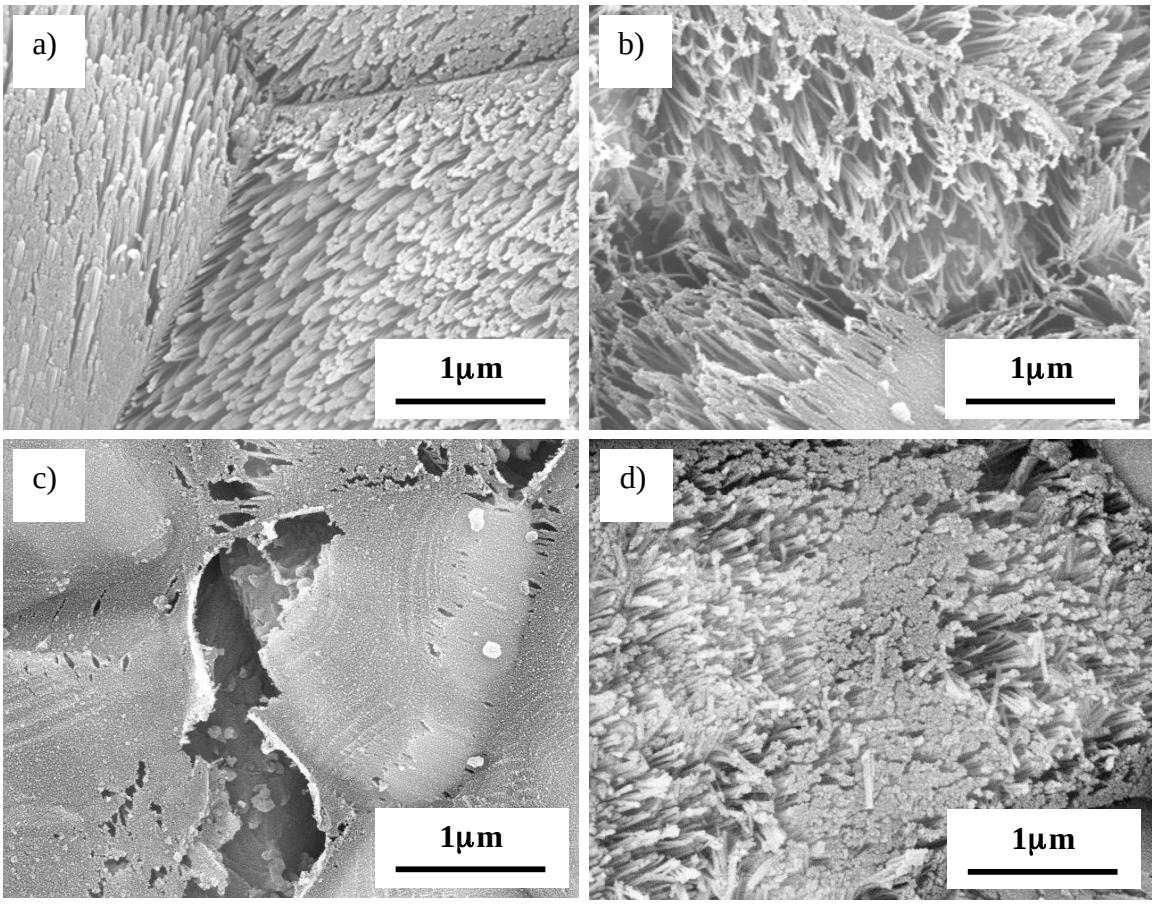

Figure 2.11: SEM images of the surfaces of TiO_2 disks after having been etched at 700°C for 8 h using (a) 1%H_2 99%N_2, (b) 5%H_2 95%N_2, and (c) 10%H_2 90%N_2; and (d) for 2 h at 700°C using 10%H_2 90%N_2 using a flow rate of 1 slpm in all cases.

A convincing piece of evidence that supports Yoo *et al.*'s titanium solid-state diffusion theory comes form mass spectroscopy data. No titanium species were found in the analysis of the exhaust gases during the nanocarving processes as illustrated in Figure 2.7. The disk samples were inspected in the SEM afterwards and it could be seen that fiber formation had occurred. ICP analyses were also performed on cotton swabs used to swab the interior of the reaction tube upstream of the mass spectrometer. Here also, no condensed titanium was found which could be attributed to the etching process. ICP analyses indicated the same amount of TiO_2 in both the cotton swabs that were not used to swab the tube, and the actual test cotton swabs that had been used to thoroughly swab out the interior of the tube. The Ti found in both sets of samples is present in all cotton swabs (it gives them their white color).

In the original paper published by Yoo *et al.*, nanoparticles at the ends of nanofibers were discovered during TEM analysis. The nanoparticles contained nickel and iron [6]. It is theorized that these particles diffuse out of the bulk TiO_2 at elevated temperatures and act as catalysts for nanofiber formation. An increase in the catalytic activity TiO_2 is typically observed for increased Fe loading [11]. Other impurities existing in the starting powder were not found in the nanoparticles [6]. To investigate this phenomenon, TiO_2 disks were doped with 0.1-mole % Fe. Large grained samples (13.28 μm) were prepared and etched using standard procedures. Fiber formation was found to occur on Fe-doped samples with large grains (13.28 μm), but not significantly on undoped samples. Although the diffusion path to the grain boundary was relatively long, Fe-doping may have promoted nanofiber formation due to its effect on diffusion. Yoo *et al.* demonstrated that nanofiber formation did not occur in samples made from

powders that were almost free of Fe impurities [7]. While Fe-doping appears to improve fiber formation the specific mechanism for such enhanced fiber formation remains unknown.

Diffusion of Fe (as $Fe^{=2}$ or $Fe^{=3}$) through the TiO_2 rutile lattice has been studied extensively [9, 12, 13]. The rapid diffusion of Fe^{2+} along the c-axis of the rutile structure explains the large difference in the diffusion rate parallel and perpendicular to the c-axis; i.e., diffusion parallel to the c-axis is greater than diffusion perpendicular to the c-axis by a factor of 1000 at elevated temperatures and low oxygen partial pressures [9]. Titanium cation self-diffusion on the other hand exhibits very little anisotropy. Ti^{4+} and Ti^{3+} interstitials are considered to be the dominant ionic defects in TiO_2 at low oxygen partial pressures [13]. We therefore propose the following theory. In the case of small grains, the titanium interstitial ions are able to diffuse to the grain boundaries and be carried away rapidly. In large grain samples, the titanium interstitials linger in the <001> diffusion channels, due to the lack of rapid diffusion via a grain boundary, and inhibit their own diffusion owing to a blocking effect in the diffusion channels. With an increased amount of Fe atoms in substitutional sites, the titanium interstitials, which are easily able to force the Fe atom into the diffusion channel, have more cation sites to jump in to as opposed to being stuck in the channels. The Fe atom then rapidly diffuses up the diffusion channel and onto the disk surface. This eliminates blocking within the channels, thereby allowing titanium interstitial diffusion to continue uninhibited. On the surface, these nanoparticles then behave as catalysts to initiated fiber formation.

2.5 Conclusion

The influences of several experimental parameters on nanofiber formation on the surface of TiO_2 disks using hydrogen bearing gas have been investigated. The titanium solid-state diffusion theory proposed by Yoo *et al.* appears to be valid. The effects of grain size and reaction gas variations appear to support this theory. Exhaust MS and ICP analyses found no volatile Ti containing species present during etching. Fe-doping appeared to have a positive effect on fiber formation. Fe-doping enabled fiber formation in large grained samples that otherwise did not form fibers. Further investigation is needed to understand the effect of iron more accurately on the nanofiber formation mechanism.

CHAPTER 3

EFFECT OF ZR-DOPING ON THE FORMATION OF TIO_2 NANOFIBERS

3.1 Introduction

Titanium dioxide (TiO_2) is a widely researched material due to its unique chemical, electrical, and optical properties. TiO_2 is chemically stable, nontoxic, and inexpensive. Its applications range from a commonly used white to possible use as a solar energy conversion surface owing to its ability to split water [8]. The thermodynamically stable form of TiO_2, rutile, has many promising industrial applications such as semiconductor electrodes for the photoelectrolysis of water and as an oxygen sensor. The surface structure of, and atomic defects/impurities in TiO_2 can significantly influence the properties this oxide [9].

Recently, a significant level of research has focused on the creation of nanostructured devices due to their potential applications in a variety of areas including photonics, electronics, and sensing [3, 4]. Precisely controlling the dimensions of such devices or their components down to the nanometer scale has proven to be quite complicated; still, some promising techniques have been discovered. Yoo *et al.* reported on the formation of nanofibers on the surface of TiO_2 polycrystalline disks using a simple gas/solid reaction process. By flowing a hydrogen bearing gas over the TiO_2 surface at an elevated temperature (700°C), nanofibers oriented along the c axis of the rutile grains

formed over the entire disk surface [6]. This current work details the effect of isovalent doping, more specifically zirconia doping, on fiber formation on polycrystalline TiO_2 disk surfaces.

3.2 Experimental Methods

Zr-doped TiO_2 powders were synthesized by hydrolysis and condensation of zirconium (IV) n-propoxide in a TiO_2 powder mixture. TiO_2 powder (Anatase, 99.9%, Alfa Aesar, Ward Hill, MA, USA) having average particle size of 32nm and zirconium (IV) n-propoxide $Zr[O(CH_2)_2CH_3]_4$ (70% in n-propanol, Alfa Aesar, Ward Hill, MA, USA) were used to synthesize the powders used in this work. The final ZrO_2 content of the raw starting material (zirconium (IV) n-propoxide in propanol) was determined using thermograviometeric analysis (Jupiter 449c, Netzsch, Germany). The raw starting material was weighed, placed in Al_2O_3 crucible, and heated to 1000°C (10 °C/min) to burn off all organic compounds. The concentration of ZrO_2 in the raw starting material was determined to have been 27.4 weight-percent.

To make doped powders zirconium (IV) n-propoxide was first dissolved in anhydrous ethanol. TiO_2 powder was added to the solution in different amounts to obtain 0.5, 1.0, 1.5, and 2.0-mol% Zr-doped titania powder. The solution and TiO_2 powder were stirred using an electrothermal mantel equipped with a magnetic stirrer for 2 hours to allow for uniform mixing. Hydrolysis of the zirconium (IV) n-propoxide was achieved by slowly (1 ml/min) adding excess amounts (10 ml) of deionized (DI) water (NANOpure Diamond Life Science (UV/UF), 18.2 MΩ-cm resistivity H_2O, 0.2 μm

filtered, Barnstead International, Dubuque, Iowa) to the solution while continuing to stir vigorously. Under uninterrupted stirring, the solution was heated to 60°C and allowed to dry for 24 hours.

Dried powders were placed in a titanium tube (Grade 2 purity in accordance with ASTM B338-05a) and calcined in a horizontal tube furnace (Lindberg/Blue M Tube Furnace, Asheville, NC, USA) at a heating rate of 5-10°C per minute in air to 600°C and holding at this temperature for 1. To break up agglomerates, powders were mixed with acetone and ground using a granite mortar and pestle. Powders were passed through 170-mesh sieve (U.S. Standard Sieve Series, Dual MFG, Co., Chicago, IL, USA) to eliminate larger particles found in the calcined powder so as to achieve increased density in the final product. Powders were pressed into disks using a 12.7 mm diameter stainless steel die (Carver, Inc, Wabash, IN, USA). The peak stress reached during uniaxial pressing was 400 MPa. The disks were sintered in air at 1200°C for 6 hours. Samples were allowed to furnace cool to room temperature.

X-ray diffraction (PW 1800 X-ray Diffractometer, Phillips, USA) analyses were preformed on samples doped with 0.5-2.0 mol-% zirconium and an undoped sample to confirm the doping concentration and to insure that the only phase present was a solid solution of zirconia in rutile titania as predicted by the phase diagram [10]. The XRD patterns, shown in Figure 3.1, were obtained using Cu Kα1 radiation at 40 kV and 30 mA with a scan rate of 0.020° step/sec from 20° to 80° 2Ω. Sample disks (undoped and 0.5, 1.0, 1.5, and 2.0-mole % Zr-doped) were crushed into powder up using a granite mortar and pestle. Powder from the crushed disks was sprinkled on a Si(511) zero-background holder (Panalytical, Netherlands) to eliminate sample displacement affects. Silicon

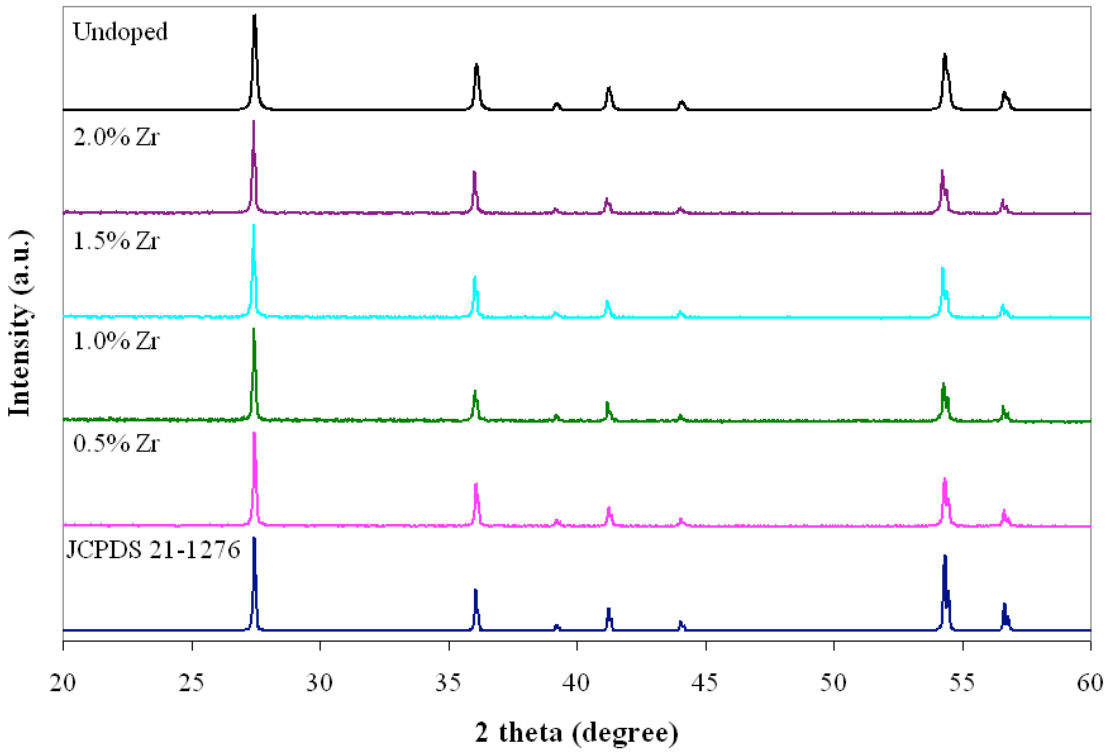

Figure 3.1: The XRD spectrums of undoped disks and doped disks with compositions ranging form 0.5 to 2.0-mol% Zr along with the JCPDS 21-1276 file for rutile TiO_2.

powder (Johnson Matthey) was used as an external standard and was x-rayed immediately prior x-raying undoped and Zr-doped crushed disks. XRD data for the Zr-doped samples was corrected for machine error calculated using the external standard. Lattice parameters for each sample were determined by using the plane spacing equation for rutile TiO_2 and Braggs Law:

$$\frac{1}{d^2} = \frac{h^2 + k^2}{a^2} + \frac{l^2}{c^2}$$; Plane spacing equation for rutile TiO_2

$$\lambda = 2d\sin(\theta)$$; Bragg's Law

By combining experimental results and Bragg's Law, d could be calculated for specific peaks in the pattern. For planes (*hkl*) with *l* equal to zero – (110), (200), (210), and (220)

– lattice parameter *a* could be calculated. For the plane having *h* and *k* indices equal to zero, (002), lattice parameter *c* could be calculated.

Individual disks were etched in a horizontal tube furnace (Lindberg/Blue M Tube Furnace, Asheville, NC, USA). After securing aluminum end-caps at both ends of the quartz tube in the furnace, a 5% H_2 95% N_2 gas mixture was passed at 1 slpm upon heating of the furnace. A typical furnace run used a 5-10°C/min heating rate to a set temperature of 700°C followed by an 8 h hold. Samples were allowed to furnace cool from the hold temperature. The 5% H_2 95% N_2 flow rate was maintained at 1 slpm throughout the run.

SEM images of the etched polycrystalline surface were analyzed by thresholding using GIMP 2.2.7, a GNP Image Manipulation Program. Four images at 6,000x magnification of each sample disk (doped and 0.5 to 2.0 mole-% Zr-doped) were analyzed for percent area etched. For each image the threshold was change to only include 105-255 pixel values, to increase the scale difference between areas missing material caused by fiber formation and unetched areas. The histogram pixel values of 0-254 were then chosen to be white and only 255 remained black to insure that black areas were due only to areas missing material due to fiber formation. The percentage of area at 255 pixel value was calculated for each sample..

Thermogravimetric Analysis (TGA) was performed on several undoped and Zr-doped samples using a Netzsch STA Jupiter 449c (Germany). Undoped disks were etching using 5%H_2 95%N_2 at 100 sccm at 700°C for 8 h in the Jupiter 449c prior to each series of 0.5, 1.0, 1.5, and 2.0 mole-% Zr-doped being etched. The 5% H_2 95% N_2 gas mixture was passed at 100 sccm starting 5 minutes prior to heating the furnace. The

furnace was heated from room temperature (~25°C) to 600°C at 40°C/min followed by a slower ramp rate of 10°C/min to 700°C to insure minimal over shooting of set temperature. Sample disks were held at 700°C for 8 h after which the furnace was cooled back to room temperature at 40°C/min while maintaining gas flow of 1 sccm of 5%H_2 95%N_2.

Sample disks were gold coated (2 min) and inspected in a scanning electron microscope (SEM) (LEO-1530 FE-SEM) to examine surface structure of etched and unetched disk. Grain sizes were calculated using a linear intercept method after ASTM E112-96(2002). Two samples of each doping level (0.5, 1.0, 1.5, and 2.0 mole-% Zr) were imaged in 4 areas at 2,000x. Each area was divided into 5 separate areas having 5 horizontal lines (~ 25 μm long and 5 μm apart) for a total of 40 inspection areas (~ 5000 grains) per doping level.

3.3 Results

X-ray diffraction (XRD) analyses were used to determine the phases present and the amount of Zr-doping in solid solution. As illustrated in Figure 3.1, the XRD spectrum remains that of rutile TiO_2 (JCPDS 21-1276) for all doping levels (i.e., a solid-solution of Zr in TiO_2 was the only phase present). Figure 3.2 illustrates the increase in lattice parameters as calculated using XRD patterns in relation to Zr-doping. As the Figure illustrates, both lattice parameters, *a* and *c*, increased with doping percentage. Similar data has been used in calculating phase diagrams [10]. The increase in lattice parameters is attributed to the size difference between the effective radii of the two

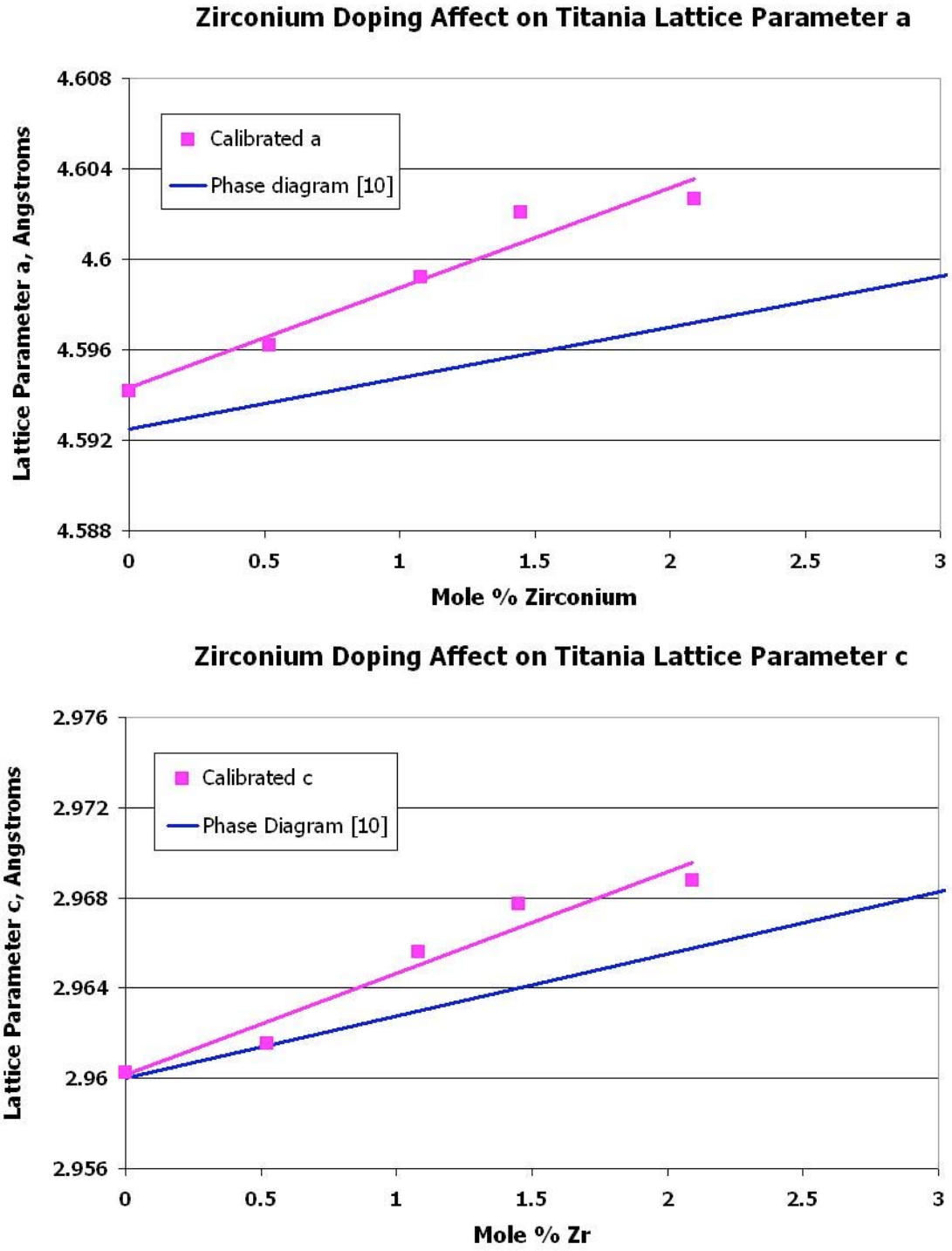

Figure 3.2: Increase in the a and c lattice parameters of rutile TiO_2 with Zr-doping concentration. Calculated a parameters (a) and c parameters (b) increase similar to data published by Brown *et al.* [10]. The "Phase diagram" lines are an approximations based on a graph published by Brown et al. depicting an increase in TiO_2 lattice parameters due to Zr-doping [10].

cations, $Ti^{=4}$(0.68Å) and $Zr^{=4}$(0.80 Å) [12, 14, 15]. The solid solubility for Zr^{4+} in TiO_2 is less then 6 mole % (much greater then the concentration of the Zr dopant used for these experiments) at temperatures lower than 900°C [10].

Grain sizes as determined by the linear intercept method and bulk density calculations are listed in Table 3.1. Grains sizes and densities as very similar to that of undoped samples, also listed on the table.

Table 3.1. Tabulation of the grain sizes (± standard deviation) and densities for sample disks having differing amounts of Zr-dopant.

Mole-% Zr doping	Average grain size (μm)	Density (% Theoretical)
Undoped	2.34 ± 0.36	92.7
0.5	2.42 ± 0.15	92.7
1.0	2.00 ± 0.12	92.2
1.5	2.11 ± 0.10	91.2
2.0	2.06 ± 0.07	89.1

Fiber formation on the surface of disks was hindered by the introduction of zirconium into the lattice. As illustrated in Figure 3.3, a decrease in fiber formation was observed with increasing zirconium content. At 0.5-mole %, fibers covered the majority of the surface (Figure 3.3a). A distinct lack of fiber formation at 2.0% doping can be seen when compared to undoped TiO_2 disks illustrated in Figure 3.4, and lesser doping amounts (Figure 3.3a-c).

Image analysis performed using GIMP 2.2.7 software also indicated a difference in the percentage of etched areas for each sample (doped and undoped). The percent black (etched area) for each sample was 0.5, 0.8, 2.2, 5.5, and 15.6 for 2.0, 1.5, 1.0, 0.5 mole-% Zr-doped, and undoped, respectively. Although the numbers do not reflect the amount of fiber formation as seen by visual inspection, each sample was analyzed using the same method, and, therefore, the data can be used as a comparison between these

samples. A representative starting image and the final analyzed image are shown in Figure 3.5.

TGA analysis of doped and undoped samples indicated weight loss for all samples. For each doping percent 3 disks were analyzed using thermogravimetric analysis. Figure 3.6 illustrates the weight loss versus time of a series of samples undoped and 0.5 to 2.0 mole-% Zr-doping. As shown, the difference in weight loss varied only slightly for each of the samples (~0.15 to 0.19 mg/cm^{-2}). Also, it should be noted that

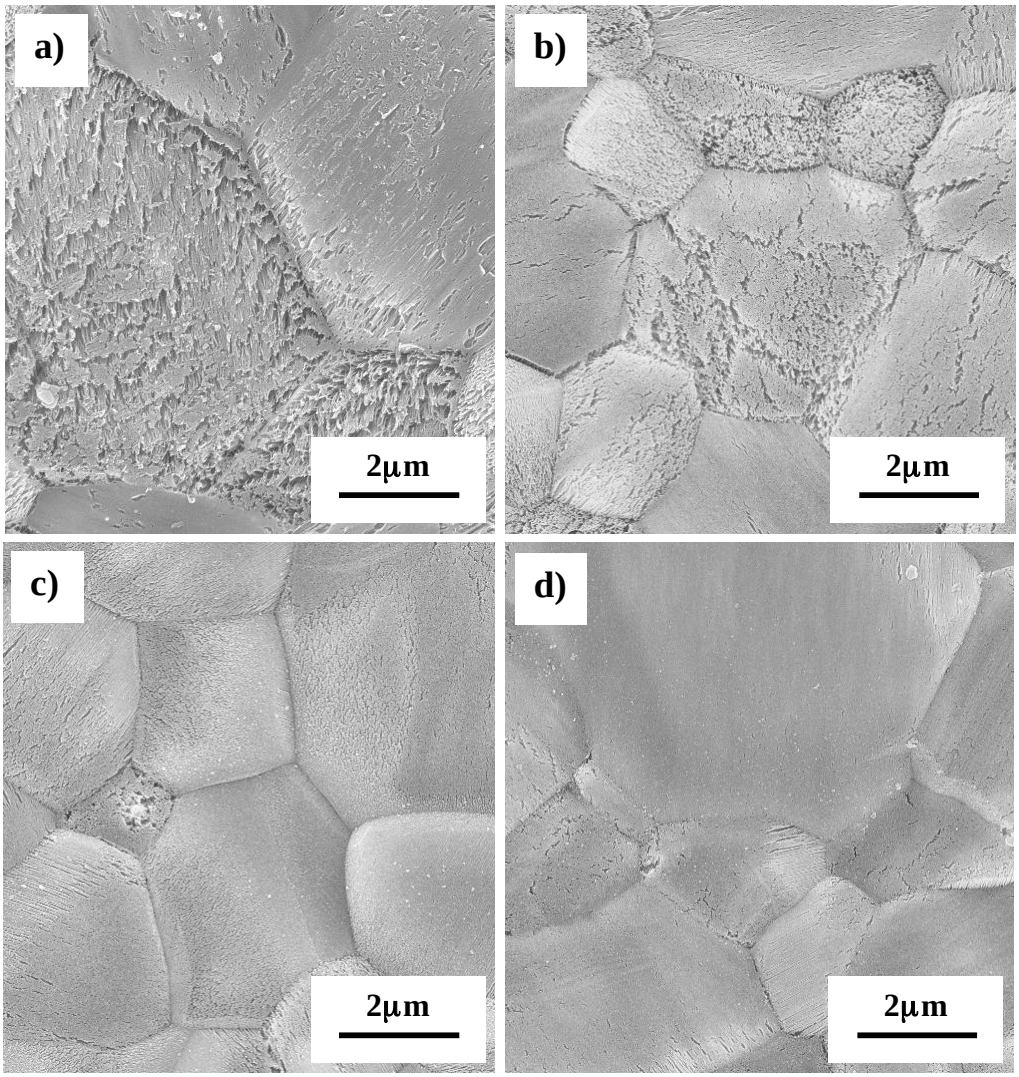

Figure 3.3: SEM images of the surfaces of TiO_2 disks doped with 0.5 (a), 1.0 (b), 1.5 (c), and 2.0 (d) mole-% Zr after etching using 5%H_2 95%N_2 at 1 slpm at 700°C for 8 h.

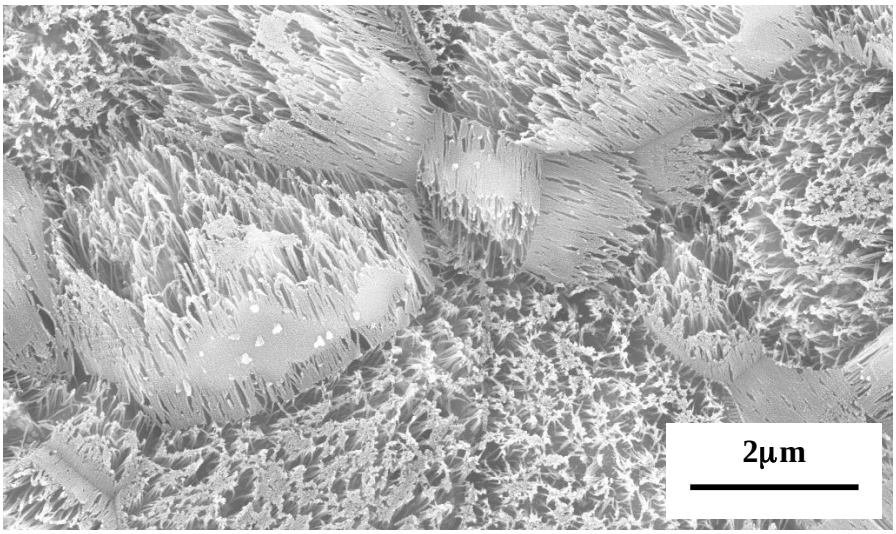

Figure 3.4: SEM image of the surface of an undoped TiO_2 disk after etching using 5%H_2 95%N_2 at 1 slpm at 700°C for 8 h.

although it appears that the undoped sample lost more weight than any of the doped samples, the weight loss of the doped samples does not decrease in the order of increasing doping percentage.

Power law and logarithmic curve fits were calculated for each doping percent. Figure 3.7 illustrates graphically the closeness of fit for each trendline. Rate constants,

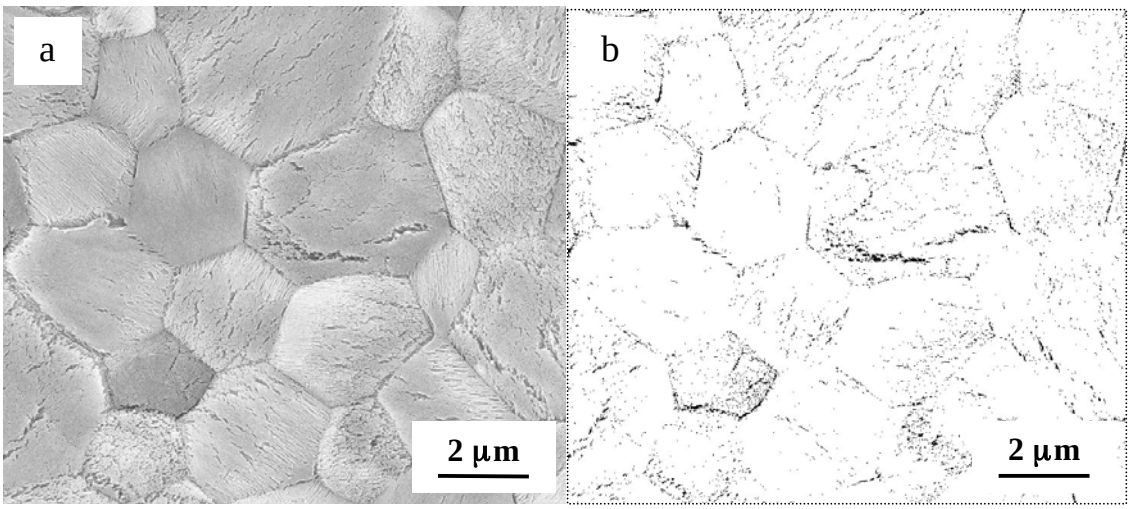

Figure 3.5: SEM image of the surface of a 1.0 mole-% Zr-doped TiO_2 disk after etching using 5%H_2 95%N_2 at 1 slpm at 700°C for 8 h (a), and after image analysis (b) using GIMP 2.2.7, a GNP Image Manipulation Program.

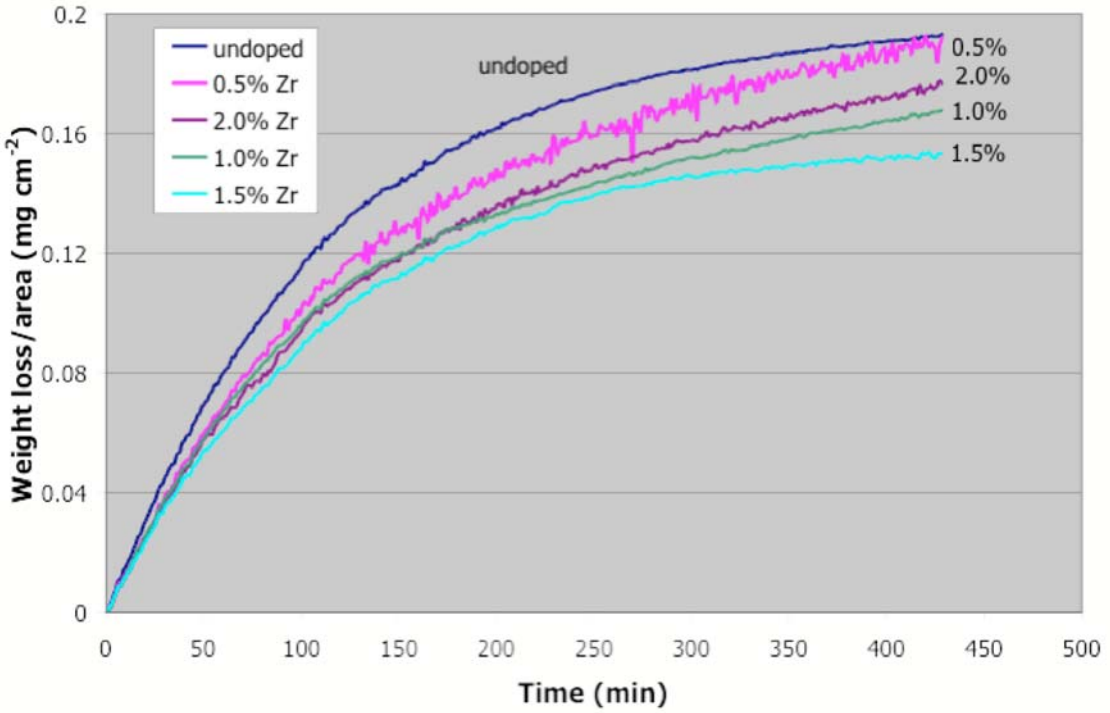

Figure 3.6: Thermogravimetric analysis of undoped and 0.5 to 2.0 mole-% Zr. Each samples was plotted as absolute weight loss per area. Time zero on the graph is 30 minutes after reaching the isothermal segment of each run.

K, were calculated for each TGA run and plot versus doping percent for logarithmic (Figure 3.8) and power law (Figure 3.9) curves. The calculated rate constants for each run (doped and undoped), including averages for each percent Zr are listed in Table 3.2. Using either rate kinetics (logarithmic or power law) there appears to be a downward trend (i.e., the rate constant decreases as Zr-doping increases). However, the difference in rate constants is minimal (less than one order of magnitude), therefore, an absolute conclusion could not be formed.

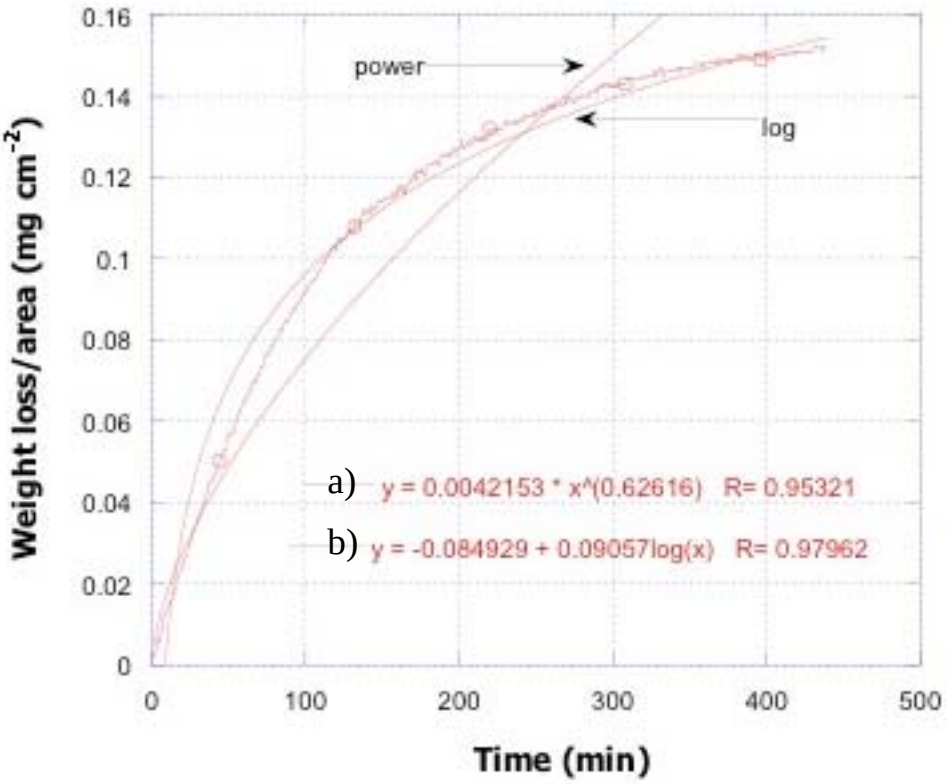

Figure 3.7: Thermogravimetric analysis of 1.0 mole-% Zr-doped sample (line with circles). Two curve fits, logarithmic and power law, are also shown on the graph. Equations, a and b, are given for the power law and the logarithmic line, respectively.

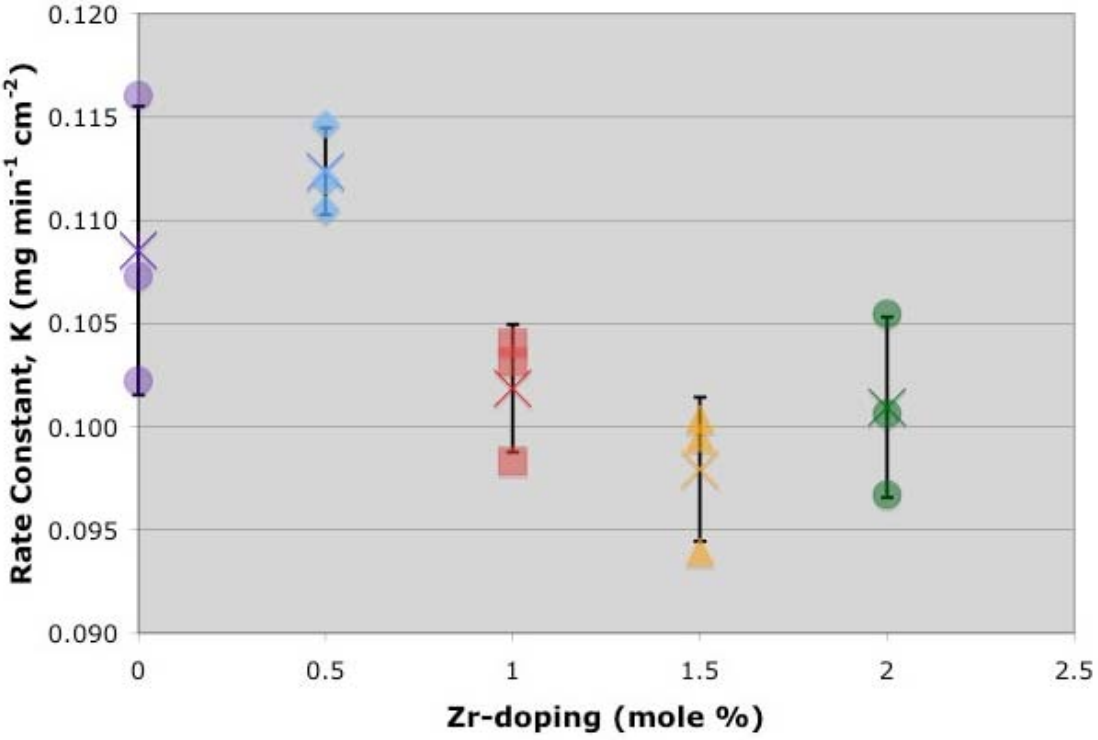

Figure 3.8: Graph of the rate constants, K, calculated for the logarithmic curve fits of each doping percent. The filled in markings represent K values for individual TGA runs. The X's and error bars are for the averages and standard deviation of each test set (3 disks for each doping percent).

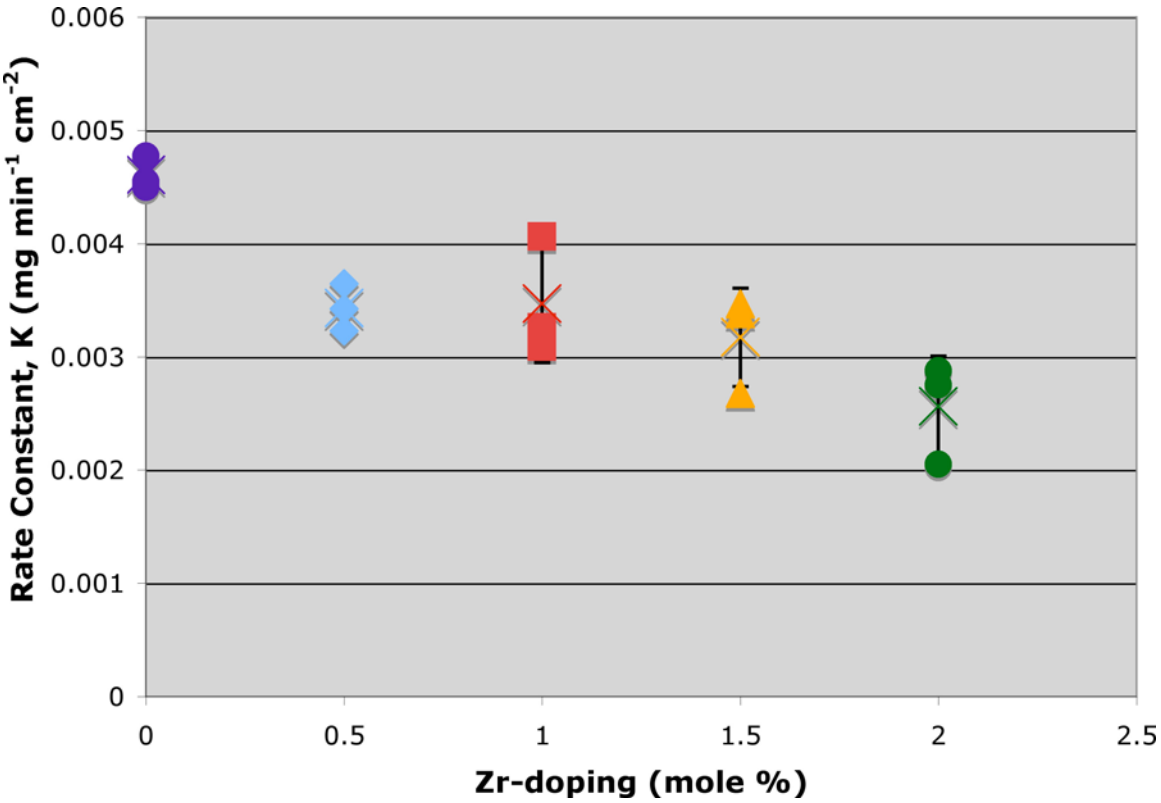

Figure 3.9: Graph of the rate constants, K, calculated for the power law curve fits of each doping percent. The filled in markings represent K values for individual TGA runs. The X's and error bars are for the averages and standard deviation of each test set (3 disks for each doping percent).

Table 3.2: Calculated rate constant values, K, for logarithmic and power law curve fits.

Sample (mole % Zr-doping, sample #)	Logarithmic Rate Constant, K	Power Law Rate Constant, K
0%, 1	0.116050	0.004549
0%, 2	0.102235	0.004772
0%, 3	0.107300	0.004497
0%, Average	0.108529	0.004606
0.5%, 1	0.111906	0.003226
0.5%, 2	0.114669	0.003421
0.5%, 3	0.110524	0.000927
0.5%, Average	0.112366	0.002525
1.0%, 1	0.103156	0.003088
1.0%, 2	0.104077	0.004061
1.0%, 3	0.098320	0.003257
1.0%, Average	0.101851	0.003469
1.5%, 1	0.099472	0.003466
1.5%, 2	0.093945	0.003379
1.5%, 3	0.100393	0.002674
1.5%, Average	0.097937	0.003173
2.0%, 1	0.096709	0.002753
2.0%, 2	0.105459	0.002878
2.0%, 3	0.100623	0.002052
2.0%, Average	0.100930	0.002561

3.4 Discussion

To explain the effects of Zr-doping on the fiber formation, it is important to consider fiber formation on undoped TiO_2 disks. Recent developments in the study of TiO_2 nanocarving have lead to a working theory behind fiber formation. Yoo *et al.* has reported on a titanium solid-state diffusion theory to explain fiber formation [7]. The reaction between the H_2 gas and the TiO_2 disks can be described by the following chemical equation:

$$TiO_2 + xH_2(g) \rightarrow TiO_{2-x} + xH_2O(g)$$

The equation implies that the surface of the disks and the composition of the fibers would not remain stoichiometric TiO_2, but some reduced form, such as Ti_2O_3 or TiO. Using XRD, XPS, and TEM analyses it was determined that this was not the case [6]. This can be explained through the solid-state diffusion of Ti^{4+} interstitials down the open channels in the c-axis of the rutile structure [7].

This theory has been validated through the combined use of Thermogravimetric analysis and mass spectrometry [7]. Thermogravimetric analysis confirmed the weight loss occurring at the surface during the nanocarving process. Combined with XRD and TEM data that indicated that both the disk surface and the individual fibers were still rutile TiO_2, it could be concluded that either a gaseous species containing titanium was leaving the surface, or that the titanium ions were diffusing back into the bulk of the disk. Mass spectroscopy of the exhaust gases of the nanocarving processes were analyzed and no titanium species were detected in the gas stream. Figure 3.10 shows a MS spectrum taken after 1 h of etching; it is representative of the entire process. Major peaks located at 28 and 44 amu correspond to N_2 and CO_2, respectively. The small peak at 29 amu adjacent to the N_2 peak was due to one of its most common isotopes. The smaller peaks, just below that of CO_2, at 40 amu and 42 amu correspond to C_2H_2N (nitrile) and N_3 (nitrogen cations). Since titanium has a molecular weight of approximately 48 amu, and no peaks were detected past 44 amu, it can be concluded that no gaseous form of titanium had formed. Therefore, Ti cations must have been diffusing back into the bulk disk.

The effect of Zr-doping of TiO_2 on nanofiber formation must be due to either a reduction of titanium solid-state diffusion or a reduction in the rate of oxygen molecules removed by the hydrogen bearing gas. Since Zr^{4+} is an isovalent dopant, it will have little

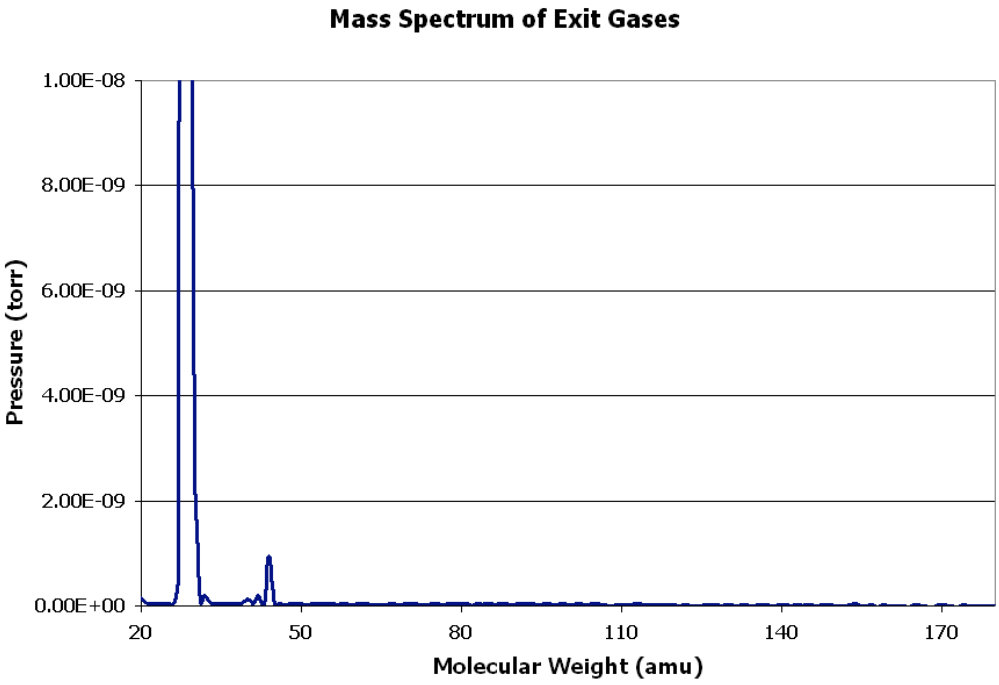

Figure 3.10: Mass spectroscopic analysis of exhaust gases during nanocarving of TiO_2 disks. The peak at 28 amu corresponds to N_2, followed by another smaller peak at 29 amu, which corresponds to a N_2 isotope peak. A CO_2 peak appears at 44 amu. No molecules containing titanium were detected.

effect on the equilibrium concentration of oxygen vacancies [14]. The lack of fiber formation on Zr-doped disks is, therefore, most likely due to the effect zirconium has on the solid-state diffusion of titanium.

Zirconium doping of TiO_2 has been examined for two main reasons: to inhibit the rutile to anatase phase transformation and to slow grain growth [14-17]. Increasing the amount of zirconium in solid solution in the anatase lattice of TiO_2 causes an increase in phase transformation temperature from around 800°C to almost 1000°C at a doping level of approximately 5-mole %. This is due to the increase in strain energy in the lattice with the incorporation of zirconium [14]. The retardation of grain growth is attributed to solute drag effects on the grain boundaries. Zirconium decreases grain boundary

mobility by a factor of ~1.5 times, which can be attributed to its relative using ionic size. Diffusion parallel to the c-axis of rutile is thought to be the rate limiting step in the solute drag process [15]. The TiO_2 rutile structure has "open" diffusion channels with a radius of ~0.77 Å that run parallel to the c-axis [2, 7]. These diffusion channels typically lead to very anisotropic diffusion coefficients for most impurities/dopants. Impurities such as Li, Fe, Co, Cr, and H diffuse much more rapidly parallel to the c-axis of rutile than perpendicular to it [9]. The strong anisotropy is attributed to the effective ionic radii of the aforementioned cations being less than that of the diffusion channel and, therefore, they can diffuse rapidly through an interstitial diffusion mechanism although they originally occupy substitutional titanium cation sites [9].

Zirconium cations, on the other hand, have an effective ionic radius of 0.80Å, which is larger than that if the diffusion channels [9, 12, 13]. Zirconium cations diffuse by an interstitialcy mechanism, which involves the simultaneous and cooperative movement of titanium cations. This is much slower than interstitial diffusion in which the atoms are simply pushed into the interstitial "open" channels and diffuse unobstructed. In fact, zirconium cations actually diffuse more quickly perpendicular to the "open" channels along the c-axis of rutile than parallel to it [9]. As previously mentioned, the slow diffusion along the c-axis could be the limiting factor in grain boundary mobility [15].

Zirconium doping may inhibit titanium diffusion along the c-axis, which occurs more rapidly than that of zirconium; i.e., the diffusion of zirconium cations down the c-axis ma be the limiting factor in the diffusion rate of this system. This can be used to explain the lack of fiber formation on the surface. Also, the presence of zirconium in the

diffusion channel or adjacent to it may also block the passage of titanium interstitials completely or inhibit it by making the channel narrower.

CHAPTER 4

SELECTIVE FORMATION OF ORIENTED SUB-MICROMETER SIZED CHANNELS ON TIO_2(001) CRYSTAL SURFACES USING HYDROGEN BEARING GAS

4.1 Introduction

Titanium dioxide (TiO_2) is a widely researched material due to its unique chemical, electrical, and optical properties. TiO_2 is chemically stable, nontoxic, and inexpensive. Its applications range from a commonly used white to possible use as a solar energy conversion surface owing to its ability to split water [8].

TiO_2 is amongst the most investigated single-crystal systems of all metal oxides. Much literature on the (110), (100), and (001) planes of the rutile phase has been published [1]. Useful techniques for changing the surface structure are of great importance due to the dependence of chemical reactions on the morphology of the surface and have, therefore, received attention in recent years [18]. The surface of TiO_2 can be complex owing to the many oxidation states of titanium and many defect structures often present [19]. Recently, it has been reported that a “nano-honeycomb” structure can be created on the surfaces of polycrystalline and single-crystal TiO_2 using photoelectrochemical etching [18, 20-23]. Sub-micrometer porous structures have been discovered after prolonged photoetching. Such structures are important due to the high crystallinity of the surface as opposed to other porous structures composed of poorly

crystallized particles [21]. This current work details a gaseous etching technique, which produces structures similar to those produce via photoelectrochemical etching.

4.2 Experimental Methods

Single-crystal TiO_2 (rutile, 99.98%) wafers with dimensions of 5mm x 5mm x 0.5mm, having 99.98% purity, and oriented in the <001> with both (001) faces polished were obtained from MTI Corporation (Richmond, CA, USA). According to manufacturer's inspection, each wafer was oriented within ±0.5 degrees of the (001) plane with a surface roughness of <5Å. Individual square samples were obtained from the as-received wafers by scoring the surface with a diamond scribe and bending the wafer until it fractured.

To study the effects of surface conditions, samples were etched either as-received, after polishing with diamond grit/sandpaper, or after being mechanically scratched using a micromanipulator. Several (001) wafers were polished using 0.25 μm, 0.5 μm, 3.0 μm, 6.0 μm, and 9.0 μm diamond paste (Crystalite Corporation, Westerville, OH, USA) and Ultra Lap Diamond Extender (LECO Corporation, St. Joseph, MI, USA) on a nylon polishing cloth (LECO Corporation, St. Joseph, MI, USA). Samples were polished to introduce defects into the surface. 1200 grit SiC sandpaper was also used to roughen the surface of some of the as-received wafers. Scratches oriented parallel and at a 45° angle to the edges of as-received wafers were also introduced with a micromanipulator (350 Probe Master, The MicroManipulator Company, USA) using a tungsten carbide probe tip (Model # 7D, tip radius 5.0 μm, The MicroManipulator Company, USA). To remove

polishing/scratching debris, samples were cleaned using dishwashing liquid soap, thoroughly rinsed using methanol, ultrasonicated in deionized (DI) water for 5 minutes, and dried using pressurized air. Prior to etching the surface roughnesses of diamond or SiC polished samples were obtained using an Atomic Force Microscope (AFM) (Nano-R AFM, Pacific Nanotechnology, USA). Not all of the samples were polished prior to etching heat treatments. A number of samples were heat treated in the as-received state.

Individual samples were placed in a horizontal tube furnace (Lindberg/Blue M Tube Furnace, Asheville, NC, USA). After securing aluminum end-caps at both ends of the quartz tube in the furnace, a 5%H_2 95%N_2 gas was passed at 1 slpm upon heating of the furnace. A typical furnace run used a 5-10°C/min heating rate to a set temperature of 1000°C followed by a 4 h hold. Samples were allowed to furnace cool from the hold temperature. The gas flow rate was maintained at 1 slpm throughout the run. Various hold temperatures (700°C, 800°C, 900°C, 1000°C) and times (2-8 hours) were also studied. After removal from the furnace, samples were gold coated for 2 minutes and the top surface (surface facing upward in the furnace) was inspected using a scanning electron microscope (LEO-1530 FESEM) at 15 kV.

Several samples underwent numerous heat treatments at various hold temperatures and times, and were viewed intermittently in the SEM to analyze development of surface structure. Samples that underwent subsequent heat treatments after having been viewed in the SEM were etched using a potassium iodide solution to remove the gold coating. Solid potassium iodide and solid iodine (both, Alfa Aesar, Ward Hill, MA, USA) were dissolved in purified DI water at a weight ratio of 4:1:40 ($KI:I_2:H_2O$). Samples were ultrasonicated in the gold etchant for five minutes, rinsed

with DI water, and dried with pressurized air prior to placement into the furnace for succeeding heat treatment(s). The gas mixture and flow rate, along with standard handling procedures (placement in furnace, removal of gold coating, etc.) remained the same for all samples. A list of samples and their surface treatments, hold temperatures, and SEM inspection history are given in Table 1. Hold times with asterisks next to them indicate that these samples were removed from the furnace following this hold time, gold coated, and viewed in the SEM prior to the next etch treatment.

Table 4.1. List of samples, their surface treatments prior to etching and the various hold temperatures used for specific sample during etching.

Sample	**700°C (hrs)**	**800°C (hrs)**	**900°C (hrs)**	**1000°C (hrs)**	**Surface treatment prior to heat treatments**
WAF 1	8*	4*	8*	8*	As received.
WAF 2	-	-	-	8*	As received.
WAF 4	2	2	2	4*	As received.
WAF 5	4	4	4	4*	As received.
WAF 6	6	6	6	6*	As received.
WAF 7	8	8	8	8*	As received.
WAF 8	-	4*	8*	8*	As received.
WAF 9	-	-	8*	8*	As received.
WAF 10	8	4	8	8*	As received.
WAF 11	8	4	8	4*	Scratched sample with 0.25μm diamond grit.
WAF 12	-	-	-	4*4*	Scratched sample with 0.25μm diamond grit.
WAF 13	-	-	-	4*	Was nano-indented prior to etching.
WAF 15	-	-	-	8*	Scratched sample with 0.25μm diamond grit.
WAF 16	-	-	-	4*	Scratched sample with 0.5μm diamond grit.
WAF 17	-	-	-	4*	Gold coated and etched in K/KI solution 4 times consecutively.
WAF 18	-	-	-	4*	As received.
WAF 19	-	-	-	4*	Scratched sample with 0.5μm diamond grit.

Table 4.1 (continued).

WAF 20	-	-	-	4*	Scratched sample with 0.5μm diamond grit.
WAF 21	-	-	-	4*	Scratched sample with 3.0μm diamond grit.
WAF 22	-	-	-	4*	Scratched sample with 6.0μm diamond grit.
WAF 23	-	-	-	4*	Scratched sample with 9.0μm diamond grit.
WAF 24	-	-	-	4*	Scratched sample with 1200 grit sandpaper.
POL 1	-	-	-	4*	Scratched sample with 0.25μm diamond grit.
POL 2	-	-	-	4*	Scratched sample with 0.5μm diamond grit.
POL 3	-	-	-	4*	Scratched sample with 3.0μm diamond grit.
POL 4	-	-	-	4*	Scratched sample with 6.0μm diamond grit.
POL 5	-	-	-	4*	Scratched sample with 9.0μm diamond grit.
POL 6	-	-	-	4*	Scratched sample with 1200 grit sandpaper.
SCR 1	-	-	-	4*	Scratched sample using micromanipulator.
SCR 2	-	-	-	4*	Scratched sample with diamond scribe.

Transmission Electron Microscopy (TEM) was performed using a Phillips CM200. The cross-section for TEM was prepared by Focused Ion Beam milling (FIB, DB235, Philips). After FIBing, the cross-section was plucked by a glass needle, placed on a TEM grid, and carbon coated. Energy Dispersive Spectroscopy (EDS) was performed on samples during TEM analysis.

4.3 Results

Figure 4.1 illustrates the progressive surface structure of a single-crystal after heat treating at 700°C for 8 h, 800°C for 8 h, 900°C for 4 h, and 1000°C for 8 h in the as-received condition under a flowing 5%H_2 95%N_2 gas mixture. The 700°C (Figure 4.1a) heat treatment had no significant effect on the surface structure of the wafer, other than a color change from a clear, slightly yellow color to a gray opaque color. This color change was attributed to the partial reduction of the TiO_2 surface [2]. The second heat treatment at 800°C resulted in nano-sized pyramidal pits on the surface of the wafer. In the succeeding treatment at 900°C (Figure 4.1c), the pits had grown to be several hundreds of nanometers in width, with some exceeding 1 micron. The pyramidal pits appeared to be overlapping and impinging upon one another. Following the final heat treatment step at 1000°C for 8 h, the surface was covered with square etch pits.

The aforementioned sample was examined using TEM to determine the orientation of the walls of the channels. The square pits extend into the wafer along the <001> direction. TEM analysis shown in Figure 4.2 determined that the sidewalls of the channels were {110} planes. As can be seen in the TEM image and other previous SEM images (Figure 4.1d), the walls of the channels were not atomically flat. The faces that were exposed were closest to the {110} planes. Upon closer inspection, it should be noted that some walls visible within the pits were parallel to the diagonal of the square holes on the surface. The planes that form the diagonals of the channels were therefore

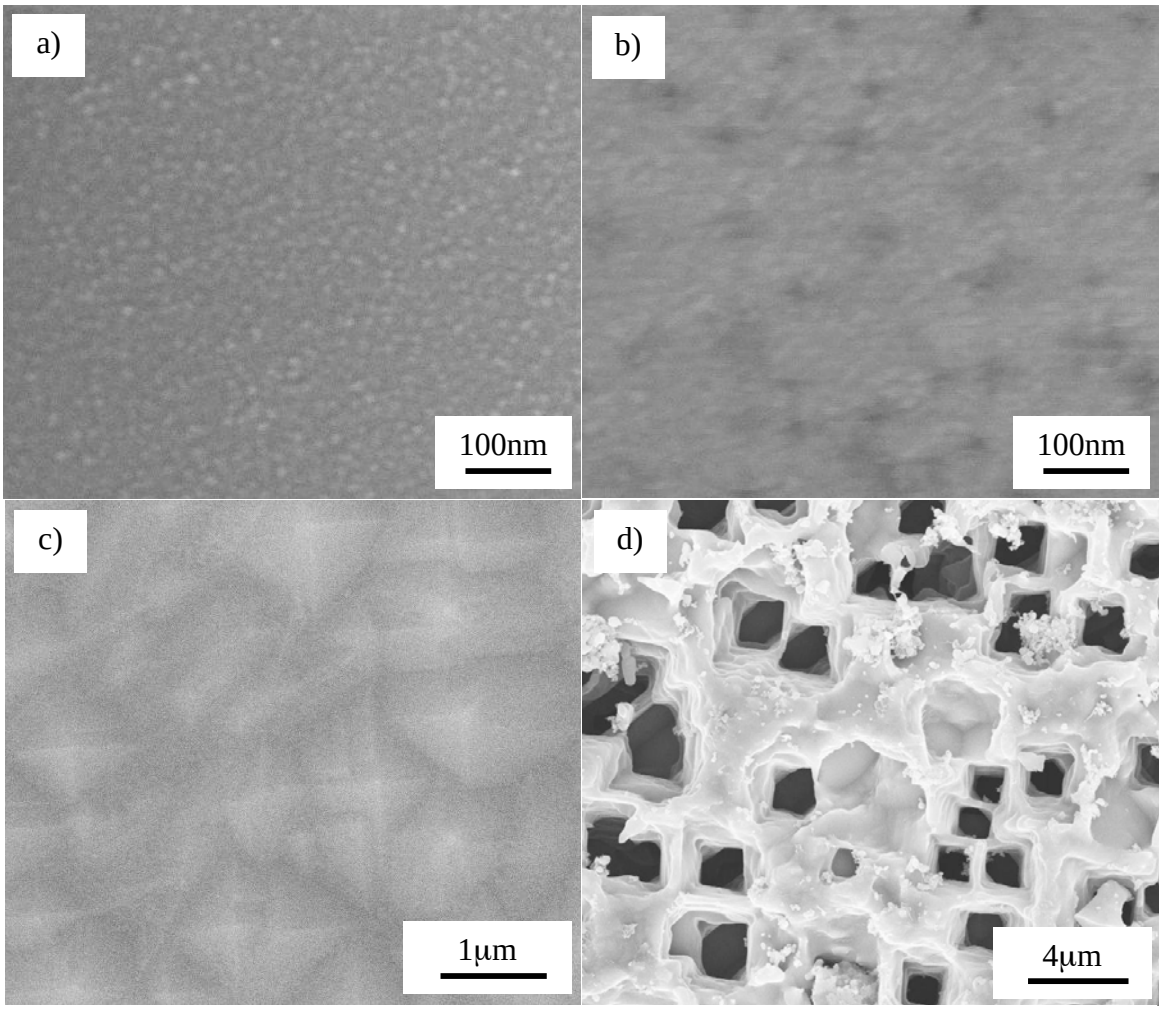

Figure 4.1: SEM images of TiO_2(001) wafer, WAF1, after undergoing successive heat treatments at (a) 700°C, (b) 800°C, (c) 900°C, and (d) 1000°C for 8 h at each temperature under 5%H_2 95%N gas atmosphere at 1 slpm flow rate.

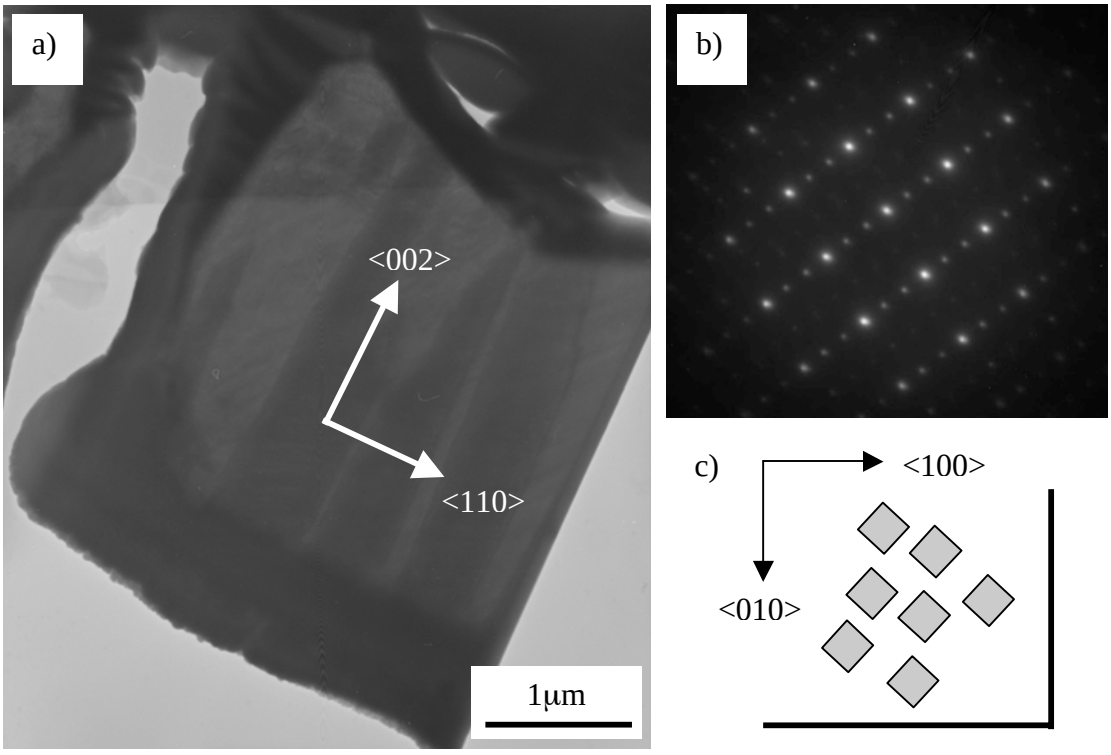

Figure 4.2: TEM analysis of as-received TiO_2(001) wafer, WAF1, that had undergone consecutive heat treatments at 700°C, 800°C, 900°C, and 1000°C in flowing 5%H_2 95%N_2 with SEM inspection at each stage. Image (a) is a TEM image of the cross section of sample. The diffraction pattern (b) of the walls of the channels shows that they are {110} planes. The orientation of the channels (gray squares) with respect to the sample edges (c) were in agreement with the diffraction pattern - the channel walls are {110} planes [7].

determined to be the (100) planes as depicted in Figure 4.3. EDS performed during TEM confirmed that only titanium and oxygen where present in the single crystal (Figure 4.4).

The same surface structures were not seen in samples that were heated directly to the different hold temperatures (i.e., not removed from furnace intermittently to view in the SEM) form the as-received condition. It was theorized that the gold coating removal process resulted in scratches on the sample surface. To examine this possibility, scratches were introduced into as-received samples by polishing with different size diamond polishing pastes. Figure 4.5 illustrates the difference after heat treating at 1000°C for 4 h in flowing 5%H_2 95%N_2 gas between a sample whose surface was scratched using 0.5 μm diamond paste prior to heat treatment (a) and one that was placed in the furnace in the as-received state (b). The surface of the wafer that was scratched prior to heat treating (Figure 4.5a) was covered with channels oriented in the <001>

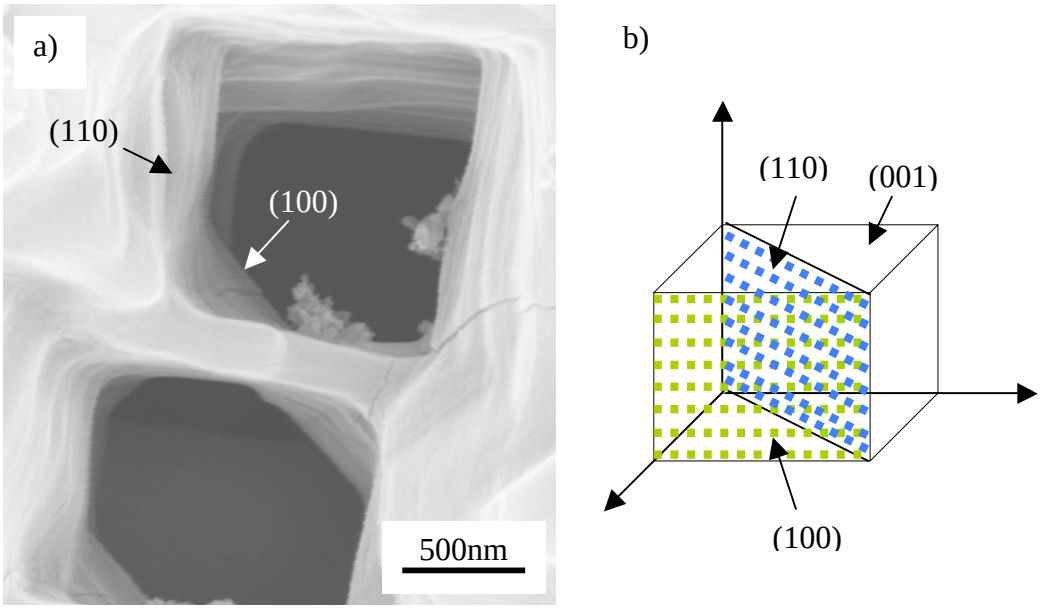

Figure 4.3: SEM image (a) of 2 channels on the surface of etched TiO_2(001) wafer, WAF1. The walls of the channels were determined to be (110) faces with (100) faces visible in the corners of the channels. Schematic (b) illustrates the different planes in the unit cell.

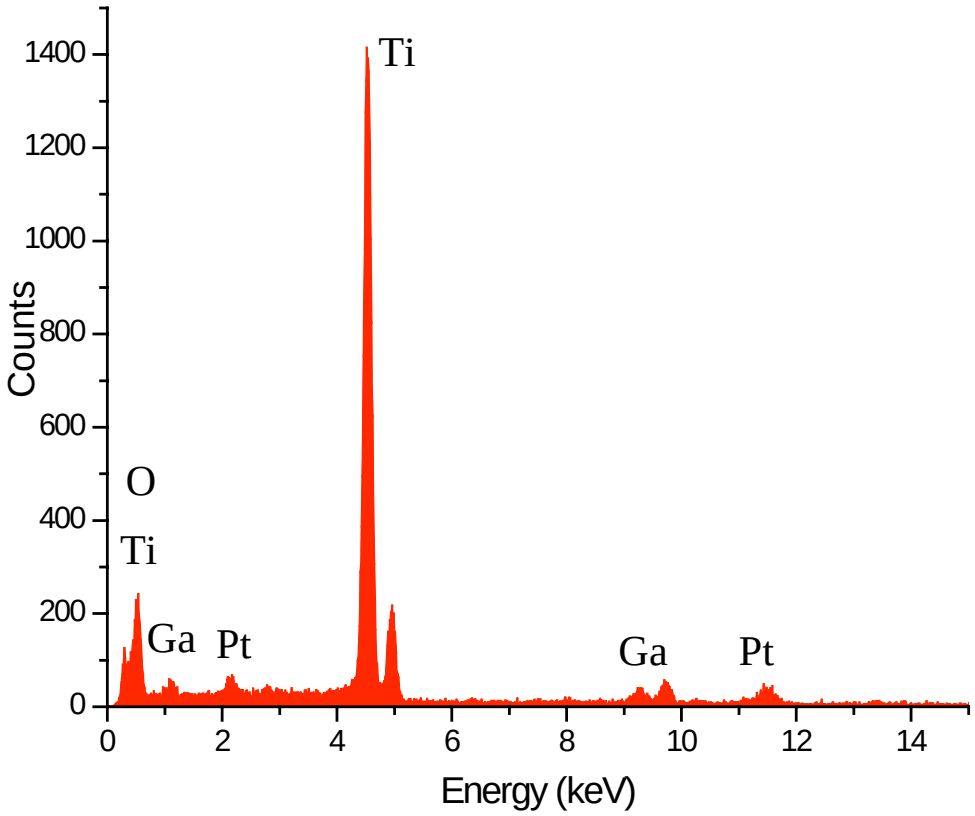

Figure 4.4: EDS spectrum of TiO_2(001) single-crystal wafer, WAF 1, after undergoing successive heat treatments at 700°C, 800°C, 900°C, and 1000°C for 8 h at each temperature under 5%H_2 95%N gas atmosphere at 1 slpm flow rate. Gallium (Ga) peaks and platinum (Pt) peaks are present due to the gallium ion beam, used to cut wafer for TEM analysis, and the conductive platinum coating applied to wafer [7].

direction. The as-received sample (Figure 4.5b) had a rough surface. However, only a few scattered channels were found on the surface upon SEM inspection. The samples were processed simultaneously (same furnace run) to assure that the heating rate and gas flow were identical for each specimen. The two samples were also pieces of the same single 5 mm x 5 mm x 0.5 mm wafer that was broken into 4 pieces prior to any surface or heat treatments.

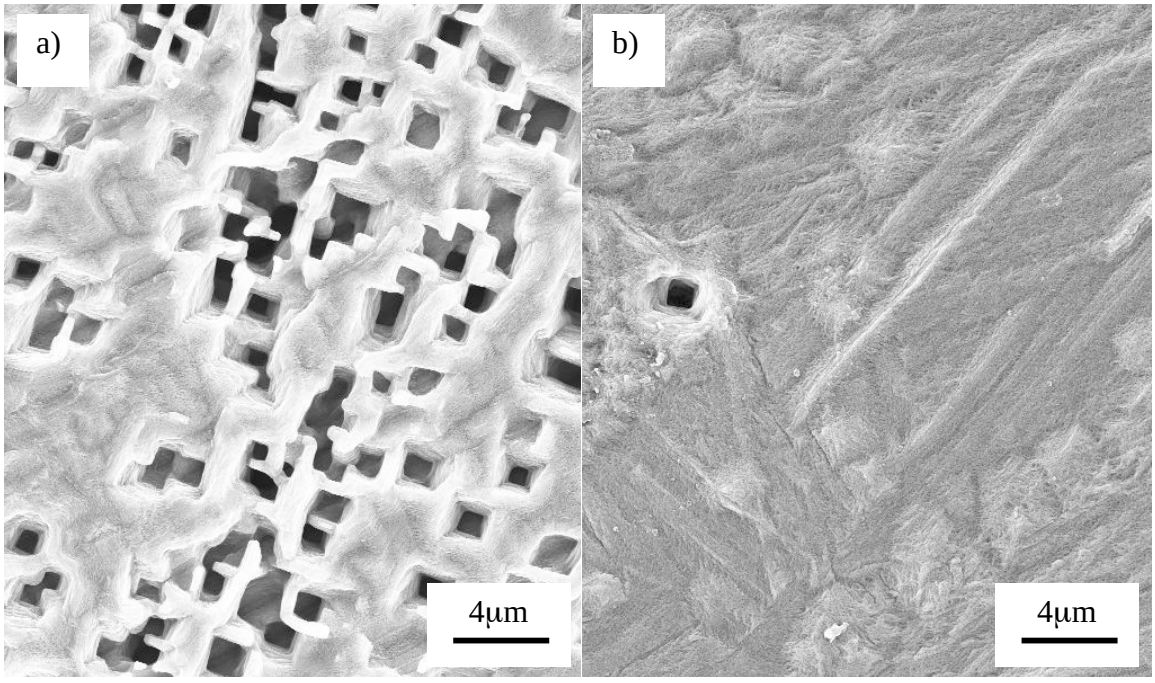

Figure 4.5: SEM images of single crystal wafers after heat treating for 4 h at 1000°C under 5%H_2 95%N gas stream having a scratched surface, (a) WAF 19, and as received polished surface, (b) WAF18, prior to heat treatment.

The surface roughnesses of samples scratched using 0.25 – 9.0 μm grit diamond paste and 1200 grit SiC sandpaper were determined using AFM prior to heat treatment (Table 4.1). Polished samples were subsequently etched using 5%H_2 95%N_2 at 1slpm for 4 h at 1000°C. The number of etch pits per square millimeter was determined using four SEM images taken at 200X of each polished wafer (~ 0.17 mm^2 per image). Surface

roughness and etch pit density are listed in Table 4.2. Along with polishing to roughen the surface, a micromanipulator was used to scratch lines at different orientations into single crystal wafers as illustrated in Figure 4.6. The etch pit density of such scratched specimens increased significantly when compared with other samples.

Table 4.2. Average surface roughness and channel density for TiO_2(001) wafers.

Polishing grit size (μm)	Average Surface Roughness (μm)	channels/mm^2
0.5	1.961	36.58
3.0	5.090	719.93
6.0	8.863	4.39
9.0	23.358	87.80
1200	49.936	95.11
Scratched	-	5162.42

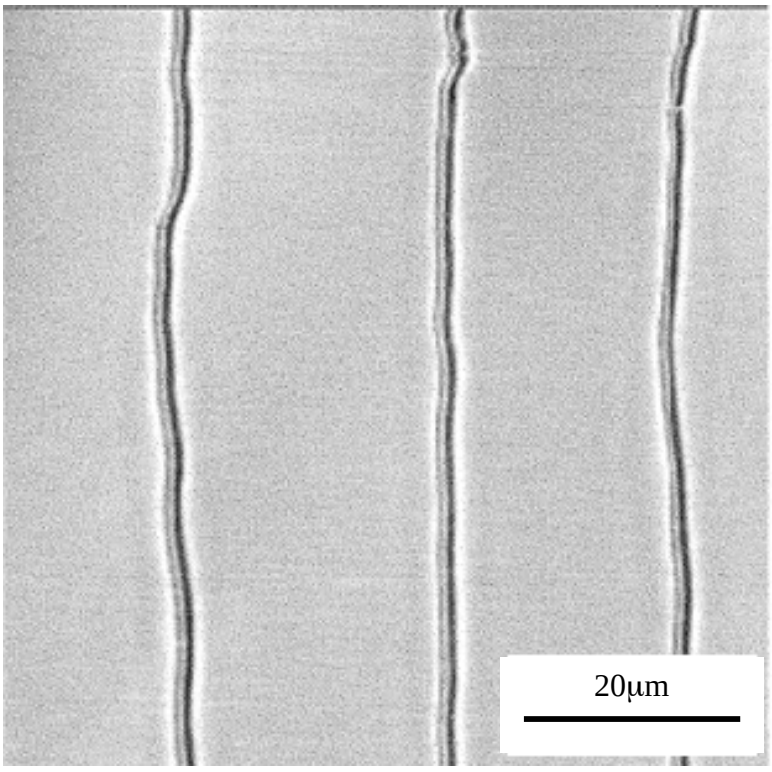

Figure 4.6: AFM image of TiO_2(001) wafer scratched using micromanipulator. Scratch width and depth are approximately 3 μm and 31 nm, respectively.

Various heat treatment temperatures and times were investigated for channel formation. An as-received single-crystal wafer was heat treated at 700°C and 800°C for 8 h each, 900°C for 4 h and 1000°C for 8 h prior to being viewed in the SEM. This treatment was identical to the sample shown in Figure 4.1 except that this sample was not allowed to cool to room temperature between heat treatments, and the sample did not undergo inspection in the SEM until after the last heat treatment. The fact that the wafer did not undergo SEM inspection between different temperature treatments meant that neither gold coating nor coating removal was ever necessary. The surface after heat treatment (Figure 4.7) did not reveal the presence of any channels. Other combinations of heat treatment temperatures and times did not lead to significant channel formation except when the surface was intentionally scratched prior to heat treatment.

4.4 Discussion

The experimental results given in the above section can be summarized as follows. Rectangular channels extending into the <001> direction, exposing the (110) faces at the walls, were created in single-crystal TiO_2(001) wafers by a combination of surface scratches and heat treatments at 1000°C in a flowing 5%H_2 95%N_2 gas mixture. The channels formed on the surfaces of the as-received wafer that was viewed intermittently in the SEM after each step of the heat treatment (700°C, 800°C, 900°C, and 1000°C) would seem to contradict the above conclusion. However, there is a simple explanation. This wafer exhibited a significant amount of channels in the <001> direction (Figure 4.1), although it had been heat treated in the as-received state (i.e., no

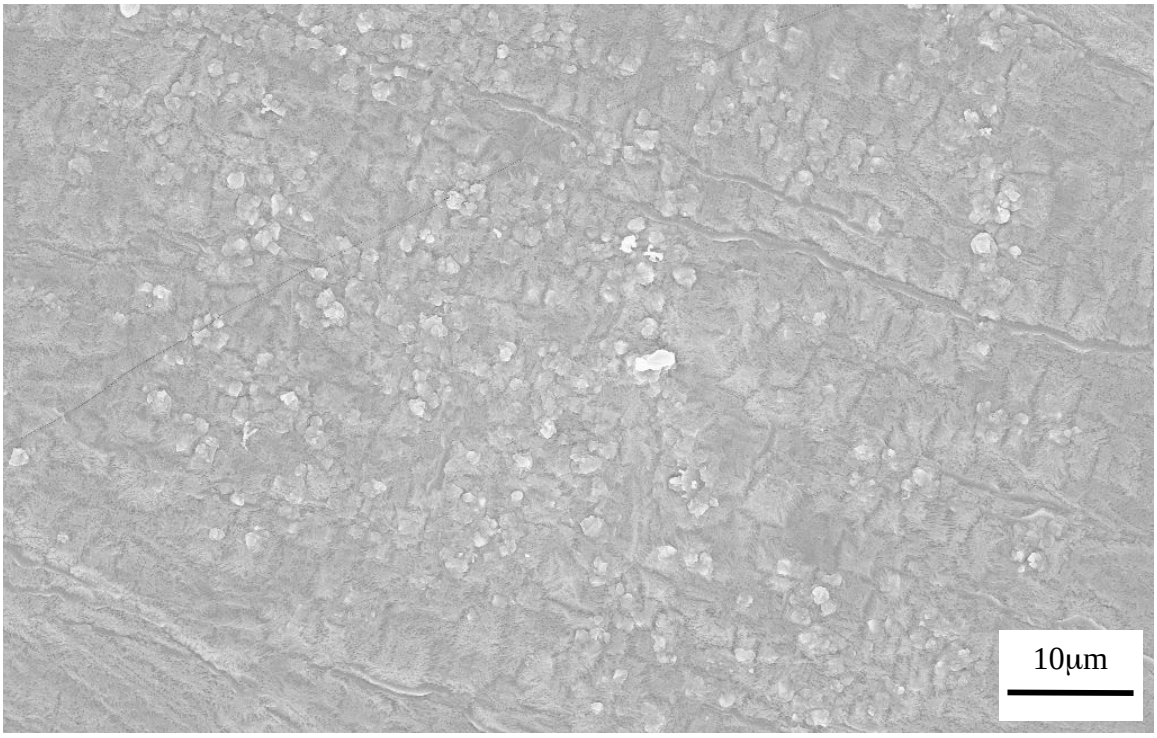

Figure 4.7: SEM image of WAF10 after heat treating at 700°C and 800°C for 8 h, 900°C for 4 h, and 1000°C for 8 h in a flowing 5%H_2 95%N_2 gas mixture without cooling or removing from furnace in between different temperatures.

scratches were made intentionally on the surface prior to heat treating). It was removed from the furnace and gold coated after each heat treatment. During the removal of the gold coating, it is likely that scratches were introduced into the surface. Figure 4.8 clearly illustrates that scratches were present on the sample during the final heat treatment, 1000°C. The channels are clearly forming along these scratches. Each time the gold coating was removed, the sample was immersed in the KI/I solution in a small beaker and ultrasonicated for 5 minutes. Collisions with the beaker most likely caused the scratches found on the surface of the wafer. Further testing of different heat treatment temperatures and times, including identical hold temperature sequences, without intermediate processing, and no prior surface treatments yielded no significant amount of channel formation on the surfaces of the single crystal samples. The variation of channel density and surface roughness (Table 4.2) suggests that the width and/or depth of scratches influenced the extent of channel formation.

Several different groups have studied the formation of etched channels in the <001> direction in TiO_2 single crystal wafers and polycrystalline samples. Sugiura *et al.* reported on the formation of a nano-honeycomb structure on the surface of polycrystalline TiO_2 disks using photoelectrochemical etching [18]. The channels were formed by immersing the titania electrodes into a 0.1M H_2SO_4 aqueous solution, illuminating the electrodes using a Hg arc lamp, and etching under a strong (+1.0V) anodic polarization condition [21]. Similar results were reported by Nakato *et al.* using single crystal wafers having (001), (100), and (110) cut and alkali-polished faces [23]. In both cases the samples were reduced, to achieve n-type semiconductivity, in a stream of hydrogen gas at 700°C prior to photoetching [21, 23]. The channels formed by

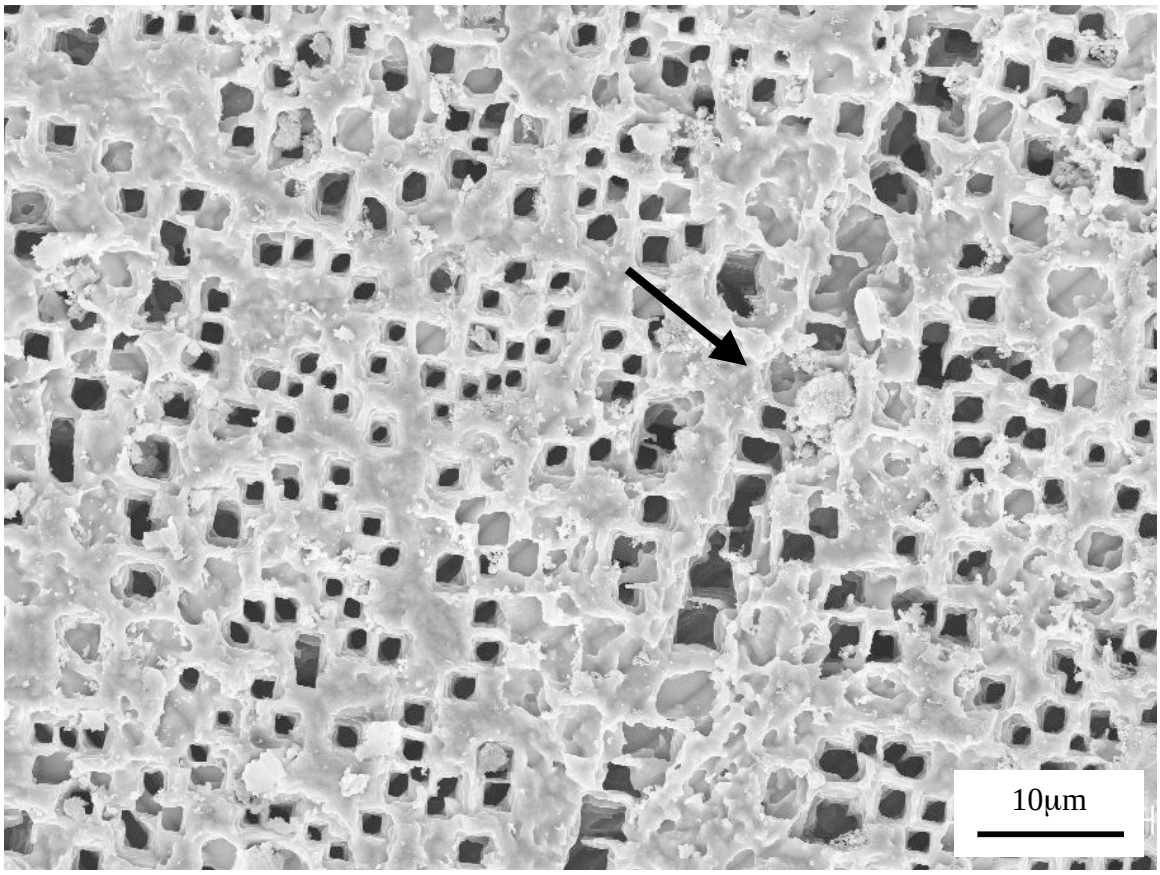

Figure 4.8: SEM image of as-received TiO_2(001) wafer that had undergone consecutive heat treatments at 700°C, 800°C, 900°C, and 1000°C in flowing 5%H_2 95%N_2 with SEM inspection at each stage after final heat treatment. The arrow indicates the location where channels were growing along a scratch in the surface.

photoelectrochemical etching on both single crystalline and polycrystalline samples were always oriented along the <001> direction. The channels ranged from 50-200 nm in edge width separated by thin (~20 nm) walls. Although, Sugiura *et al.* first reported that the walls of the channels were (110) crystal faces interconnected vertically, closer inspection revealed that the walls were actually (001) crystal faces [18, 21]. Results reported on by Nakato *et al.* also indicated that the walls of the channels in the single crystalline wafers were (001) crystal faces [23]. Nakato *et al.* have recently proposed a theory as to why the (001) crystal face is left exposed, when the (110) faces are the least thermodynamically stable. Using a series of coupling and hole-oxidation chemical equations, the process by which the holes are created was described. They believe that due to atomic grooves in the surface of the (100) faces, illustrated in Figure 4.9, the surface trapped holes are inaccessible by water and etching cannot proceed quickly at these faces [20].

The difference in orientation of photoelectrochemically etched and gas etched channels can be explained. The surface structure of the (001) crystal face is thermodynamically the least stable face, because it has the highest number of dangling bonds at the surface. The (110) face, on the other hand has the lowest surface energy and is more stable than the (100) face [1]. Annealing wafers having (001) faces leads to nonstiochiometric pyramidal facets bound by (011) planes [24]. When annealing under a stream of hydrogen gas, the facets actually become pits due to the removal of oxygen from the surface of the (001) wafer. This process continues on until long channels are formed. The location of the channels appears to be dictated by flaws in the surface of the wafer. The theory proposed by Nakato *et al.* to explain the selective etching of titania surfaces leaving the (100) crystal face exposed as the channel walls, does not apply to

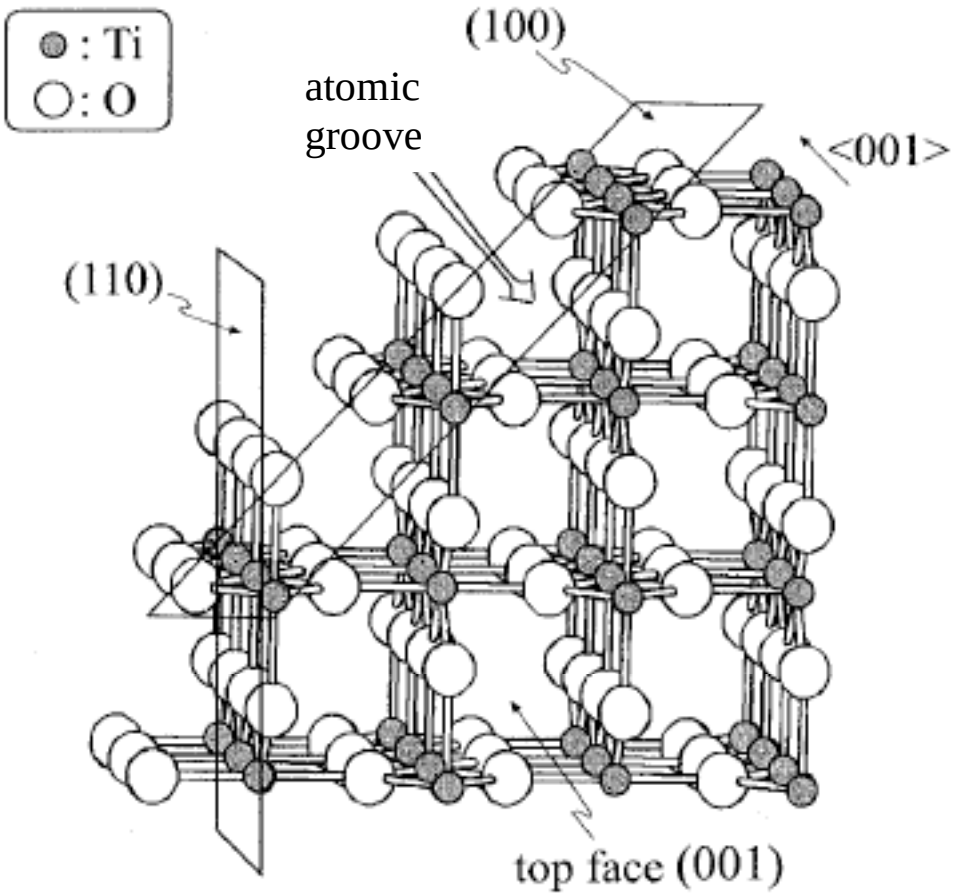

Figure 4.9: Schematic of the crystal structure of TiO_2 rutile, illustrating the (110), (100), and (001) faces. After ref. [23].

etching using hydrogen gas. The hydrogen molecules are much smaller than the water molecules needed for photochemical etching and are not impeded by the atomic groove in the (100) crystal face. The (100) surface actually has more dangling bonds at the surface, making it easier for the hydrogen to remove oxygen ions, therefore creating walls oriented mainly along (110) planes. However, there appears to be significant removal of both crystal surfaces, because the channels are not completely straight (110) oriented faces, but as illustrated in Figure 4.3, have walls further within the channel having (100) faces. Further investigation is necessary to confirm this theory.

Although the wafers examined here were not photoelectrochemically etched as with those reported previously, several important similarities exist. The channels created using either method are oriented along the <001> direction and are on similar size scales. However, the channels created by the 5%H_2 95%N_2 gas stream at 1000°C have walls with (110) crystal faces and those created using aqueous H_2SO_4 solutions have (100) crystal faces. Nakato *et al.* noted that the surface of their wafers having (001) crystal faces had sparsely distributed pyramidal pits in the <001> direction with the edges of the pits on the surface oriented along the (110) after having been reduced in a stream of hydrogen at 700°C for 30 minutes. The same type of pyramidal pits were also seen on (001) surfaces that had been chemically etched at 230°C for 30 minutes in a solution composed of H_2SO_4 and $(NH_4)_2SO_4$ in ratio of 2:1 [23]. The pits in the above cases appeared to be shallow and sparse. Sparse distribution of etch pits was discovered on our as-received samples inspected after 5%H_2 95%N_2 etching at 800°C, 900°C, and 1000°C as illustrated in Figure 4.5b. The density of the etch pits was drastically increased when scratching the surface prior to etching. The high density of the etch pits having walls that

were (110) crystal faces appear to be unique with respect to the present combination of surface treatments and hydrogen heat treatments. Unfortunately, a direct correlation between surface roughness and ending etch pit density cannot be made. As noted in Table 4.2, the etch pit density increases drastically for 3.0μm polished samples, but then decreases again as surface roughness increases. The etch density is largest, however, for wafers scratched using a micromanipulator. It seems that there maybe an optimum scratch size or density that leads to etch pit growth.

Surface structures and energetics of titania can be modified significantly by lapping or polishing. Lapping, much like argon sputtering, of the surface of titania preferentially removes oxygen from the surfaces. This increases the amount of oxygen defects at damage sites leaving behind nonstiochiometric oxidation states Ti^{+3} and Ti^{+2} [2]. The Ti^{+3} sites, defect sites, are favorable for dissociative water adsorption [16]. It is here that the hydrogen molecules adsorb into the surface of titania bonding with the remaining oxygen ions. Eventually, the –OH molecules escapes from the surface and is carried of in the gas stream. In theory, the increase in channels when scratching the surface prior to etching should be able to be explained by the change in energetics and stoichiometry at defect sites.

REFERENCES

1. Diebold, U., *The surface science of titanium dioxide.* Surface Science Reports, 2003. **48**: p. 53-229.

2. Miki, T. and H. Yanagi, *Scanning Probe Microscopic Charaterization of Surface Modified n-TiO_2 Single-Crystal Electrodes.* Langmuir, 1998. **14**: p. 3405-3410.

3. Li, D. and Y. Xia, *Fabrication of Titania Nanofibers by Electrospinning.* Nano Letters, 2003. **3**(4): p. 555-560.

4. Michailowski, A., et al., *Highly regular anatase nanotubule arrays fabricated in poruos anodic templates.* Chemical Physics Letters, 2001. **349**: p. 1-5.

5. Du, G.H., et al., *Preparation and structure analysis of titanium oxide nanotubes.* Applied Physics Letters, 2001. **79**(22): p. 3702-3704.

6. Yoo, S., S.A. Akbar, and K.H. Sandhage, *Nanocarving of Bulk Titania Crystals into Oriented Arrays of Single-Crystal Nanofibers via Reaction with Hydrogen-Bearing Gas.* Advanced Materials, 2004. **16**(3): p. 260-264.

7. Yoo, S. and S.A. Akbar, *Oral Communication*. 2005.

8. Nakamura, R., T. Tanaka, and Y. Nakato, *Mechanism for Visible Light Responses in Anodic Photocurrents at N-doped TiO_2 Film Electrodes.* Journal of Physical Chemistry B, 2004. **108**: p. 10617-10620.

9. Sasaki, J., N.L. Peterson, and K. Hoshino, *Tracer Impurity Diffusion in Single-Crystal Rutile.* The Journal of Physics and Chemistry of Solids, 1985. **46**(11): p. 1267-1283.

10. Frank H. Brown, J. and P. Duwez, *The Zirconia-Titania System.* Journal of the American Ceramic Society, 1954. **37**(3): p. 129-133.

11. Pecchi, G., P. Reyes, and R. Zamora, *Kinetics of Methane Combustion on Fe_20_3 Catalysts.* Reaction Kinetics and Catalyst Letter, 2003. **80**(2): p. 375-381.

12. Yan, M.F. and W.W. Rhodes, *Effects of cation contaminants on conductive TiO_2 ceramics.* Journal of Applied Physics, 1982. **53**(12): p. 8809-8818.

13. Peterson, N.L., *Impurity Diffusion in Transition-Metal Oxides.* Solid State Ionics, 1984. **12**: p. 201-215.

14. Yang, J. and J.M.F. Ferreira, *On the Titania Phase Transition by Zirconia Additive in a Sol-Gel-Derived Powder.* Materials Research Bulletin, 1998. **33**(2): p. 389-394.

15. Yan, M.F. and W.W. Rhodes. *Effects of Solutes on the Grain Boundary Mobility of TiO_2.* in *University Conference on Ceramics (Ceramic Microstructures '86).* 1986. Berkeley, CA: Plenum Press.

16. Wang, Y.M., et al., *Preparation and Photocatalytic Properties of Zr^{4+}-doped TiO_2 Nanocrystals.* Journal of Molecular Catalysis A: Chemical, 2004. **215**: p. 137-142.

17. Han, J.-K., et al., *Photocatalysis for Oxidation of Phenol and Reduction of Inorganic Pollutants by Nanocrystalline TiO_2-ZrO_2 Powders.* Materials Science Forum, 2004. **449-452**: p. 289-292.

18. Sugiura, T., T. Yoshida, and H. Minoura, *Microstructural Observation of Photoelectrochemically Tailored Nano-Honeycomb TiO_2.* Electrochemistry, 1999. **67**(12): p. 1-3.

19. Hoflund, G.B., et al., *Surface Study of the Oxidative and Reductive Properties of $TiO_2(001)$.* Langmuir, 1988. **4**: p. 346-350.

20. Kisumi, T., et al., *Crystal-face and illumination intensity dependences of the quantum efficiency of photoelectrochemical etching, in relation to those of water photooxidation, at n-TiO_2 (rutile) semiconductor electrodes.* Journal of Electroanalytical Chemistry, 2003. **545**: p. 99-107.

21. Sugiura, T., T. Yoshida, and H. Minoura, *Designing a TiO_2 Nano-Honeycomb Structure Using Photoelectrochemical Etching.* Electrochemical and Solid-State Letters, 1998. **1**(4): p. 175-177.

22. Sugiura, T., et al., *Evolution of a skeleton structured TiO_2 surface consisting of grain boundaries.* Journal of Electroanalytical Chemistry, 1999. **473**: p. 204-208.

23. Tsujiko, A., et al., *Selective Formation of Nanoholes with (100)-Face Walls by Photoetching of n-TiO_2 (Rutile) Electrodes, Accompanied by Increases in Water-Oxidation Photocurrent.* Journal of Physical Chemistry B, 2000. **104**: p. 4873-4879.

24. Ramamoorthy, M., D. Vanderbilt, and R.D. King-Smith, *First-principle calculations of the energetics of stoichiometric TiO_2 surfaces.* Physical Review B, 1994. **49**(23): p. 16721-16727.